Basin Research

IAS EAGE

Thermochronometry unveils ancient thermal regimes in the NW Pampean Ranges, Argentina: From Mesozoic rifting to Miocene flat-slab subduction.

Journal:	*Basin Research*
Manuscript ID	BRE-264-2021
Wiley - Manuscript type:	Research Article
Date Submitted by the Author:	16-Dec-2021
Complete List of Authors:	EZPELETA, Miguel; CONICET Cordoba Parra, Mauricio; Universidade de Sao Paulo Instituto de Geociencias COLLO, Gilda; CONICET Cordoba WUNDERLIN, Cecilia; CONICET Cordoba BORREGO, Angeles G.; Gobierno del Principado de Asturias Consejeria de Educacion Cultura y Deporte Sobel, Edward R.; Universitat Potsdam Institut fur Geowissenschaften GLODNY, Johannes; Deutsches Geoforschungszentrum Potsdam
Keywords:	Triassic Ischigualasto-Villa Union Basin, %Ro and XRD in the clay fraction, AFT, AHe and ZHe, thermochronological modelling, Triassic rifting, Cenozoic flat-slab, Cooling decupled of exhumation
Keywords:	

- %Ro, I/S data and thermochronological models shows two different stages of burial and exhumation.
- Peak temperatures during Triassic rifting, with a geothermal gradient of 45 ºC/km and high heat flow (100 mW/m^2).
- Cenozoic cooling associated with lithospheric refrigeration is due to flat-slab subduction and not to exhumation.
- Variable basal heat flow produce that thermal maxima are not associated with peak subsidence.
- Decoupling between the initial signals of cooling and exhumation is seldom documented.

Thermochronometry unveils ancient thermal regimes in the NW Pampean Ranges, Argentina: From Mesozoic rifting to Miocene flat-slab subduction.

Miguel EZPELETA [1,2], Mauricio PARRA[3], Gilda COLLO[1,4], Cecilia WUNDERLIN[* 1] Angeles G. BORREGO[5], Edward R. SOBEL[6] and Johannes GLODNY[7].

[1] Centro de Investigaciones en Ciencias de la Tierra (CICTERRA), Universidad Nacional de Córdoba, Consejo Nacional de Investigaciones Científicas y Técnicas (CONICET), Av. Vélez Sarsfield 1611, X5016CGA, Ciudad Universitaria, Córdoba, Argentina. *miguelezpeleta@gmail.com. *Corresponding author.*

[2] Departamento de Ciencias Aplicadas, Universidad Nacional de La Rioja, Luis M. de la Fuente S/N, La Rioja, Argentina.

[3] Instituto de Geociências, Universidade de São Paulo, 05508-010, São Paulo, Brazil.

[4] Departamento de Geografía, Facultad de Filosofía y Humanidades. FFyH – Universidad Nacional de Córdoba, Casa Verde, Primer Piso. Ciudad Universitaria (5000), Córdoba.

[5]Instituto de Ciencia y Tecnología del Carbono (INCAR-CSIC), Francisco Pintado Fe, 26, 33011 Oviedo, Asturias, España.

[6] Institut für Geowissenschaften, Universität Potsdam, Karl-Liebknecht-Str. 24-25, 14476 Potsdam, Germany.

[7]GFZ German Research Centre for Geosciences, Telegrafenberg, Building B, 14473 Potsdam,Germany.

Acknowledgments

We are grateful to the International Cooperation CONICET-FAPESP Project (2016, 23220160100035CO), the Agencia Nacional de Promoción Científica y Tecnológica (PICT 2015-3146, PICT 2015-1092 and PICT 2017-3177), the Proyecto de Investigación Secyt-UNLaR 2015/10736 and 2015/00422, for supporting our research work. Themochronometric analyses were funded by the FAPESP-CONICET SPRINT (Project 2016/50441-1). We would like to acknowledge the initial work of Martín Gorocito, the help of Graciela Toledo with mineral separations and of Ileana Perassi with the clay minerals concentration and analysis in the CICTERRA, and to all the members of the Low Temperature Thermochronology Laboratory of the São Paulo University, and the Instituto Nacional del Carbón (Oviedo, España).

Data Availability Statement: The data are available from the corresponding author upon reasonable request. There is no conflict of interest between authors.

Abstract

Reconstructing thermal histories in thrust belts is commonly used to infer the age and rates of thrusting and hence the driving mechanisms of orogenesis. In areas where ancient basins have been incorporated into the orogenic wedge, a quantitative reconstruction of the thermal history helps distinguish among potential mechanisms responsible for heating events. We present such a reconstruction for the Ischigualasto-Villa Unión basin in the western Pampean Ranges of Argentina, where Triassic rifting and late Cretaceous-Cenozoic retroarc foreland basin development, including Miocene flat-slab subduction have been widely documented. We report results of organic and inorganic thermal indicators acquired along three stratigraphic sections, including vitrinite reflectance and X-ray diffractometry in claystones and new thermochronological [(apatite fission-track and apatite and zircon (U-Th)/He)] analyses. Despite an up to 5 km-thick Cenozoic overburden and unlike previously thought, the thermal peak in the basin is not due to Cenozoic burial but occurred in the Triassic, associated with a high heat flow of up to 90 mWm^{-2} and less than 2 km of burial, which heated the base of the Triassic strata to ~160°C. Following exhumation, attested by the development of an unconformity between the Triassic and Late-Cretaceous-Cenozoic sequences, Cenozoic re-burial increased the temperature to ~110°C at the base of the Triassic section and only ~50°C 7 km upsection, suggesting a dramatic decrease in the thermal gradient. The onset of Cenozoic cooling occurred at ~10-8 Ma, concomitant with sediment accumulation and thus preceding the latest Miocene onset of thrusting that has been independently documented by stratigraphic-cross-cutting relationships. We argue that the onset of cooling is associated with lithospheric refrigeration following establishment of flat-slab subduction, leading to the eastward displacement of the asthenospheric wedge beneath the South American plate. Our study places time and temperature constraints on flat-slab cooling calls for a careful interpretation of exhumation signals in thrustbelts inferred from thermochronology only.

Key words: Triassic Ischigualasto-Villa Union Basin, %Ro, XRD in the clay fraction, thermochronological modelling (AFT, AHe and ZHe), heat flow, burial, Triassic rifting, Cenozoic flat-slab,

1. Introduction

The reconstruction of thermal histories in orogenic belts resulting from polyphase deformation is a key element to unveil the underlying geodynamics yet hardly accessible due to the paucity of paleothemometers in deeply eroded regions. Relicts of sedimentary basins incorporated in mildly exhumed thrustbelts, as those present in the Central Andes (eg. Jordan et al., 1993), offer an unique opportunity to investigate the ages and maximum temperatures associated with tectono-thermal events and hence help place constraints to the driving mechanisms of orogenesis. In addition, identifying the thermal trajectories in the sedimentary basins is relevant for assessing their hydrocarbon generation potential of potentially petroliferous intervals. The temperature increase is considered the main control on the maturation of organic matter in a basin, although pressure and the residence time under certain thermal conditions are also significant (Tissot et al., 1987; Ungerer et al., 1990; Schenk et al., 1997). Moreover, a number of variables such as paleolatitude, fluid flow, the chemistry of the matrix and the pore fluids can also affect the thermal history and, in consequence, the maturation rate of the organic matter (Magoon and Beaumont, 1999). In sedimentary basins, the main mechanisms that generate heating are burial, heat transfer from the asthenosphere, and magmatism, even though the latter usually is associated with restricted areas (Ungerer et al., 1990). In the Andean foreland, between 29º-32ºS (see synthesis of Jordan et al., 1993; Jordan et al. 2001), the evolution of deformed belts, such as Miocene basins, has been key to understand the evolution of the Andean orogen in the southern part of the Central Andes. These studies have allowed to relate geological, geophysical and geodynamic aspects of the segment currently affected by flat subduction (eg. Siame et al., 2005; Vergés et al., 2007, Collo et al., 2011; 2015; 2018). However, the thermal effects of flat subduction onto a continental margin that underwent Mesozoic lithospheric stretching remain to be disentangled.

The Ischigualasto Basin (Figure 1A and 1B) is part of a series of partially connected half-graben depocenters formed during a rifting period that affected this region of Gondwana from the Upper Permian to the Upper Triassic (Uliana et al., 1989). These basins are mostly limited by high-angle fault systems that showed different degrees of activity during basin development (Franzese and Spalletti, 2001: Spalletti, 2001, Melchor, 2007). The petrolific Cuyana Basin (Fig. 1B) has been the most studied and is the main reference to understand the filling and subsequent evolution of these depocenters (eg. Spalletti, 2001; Zencich et al., 2008). In the Cuyana Basin, it has been argued that the thermal maximum

was triggered and controlled by the development of a Cenozoic foreland infilling that overlapped the Triassic basin, providing the sedimentary column necessary for hydrocarbon source rock maturation during the last 10 Ma (Avila et al 2005, Zencich et al., 2008).

However, the works carried out in order to elucidate the thermal evolution of these Permo-Triassic sub-basins in the Bermejo and Ischigualsto-Villa Union intermountain region are scarce (Ortiz et al. 2015, 2021, Fosdick et al 2015). In this region, one of the thickest Neogene basins of the Andes has developed (Ramos, 1970, Jordan and Alonso, 1987). In this foreland basin, the sedimentary infill is more than 10 km thick, and specifically in this sections more than 7000 m of sediments are preserved (Rossello et al 1996, Geogieff et al 2009, Canelo et al. in press) and the top of the synorogenic sequences were eroded. The development of this foreland basin was affected by the change to a flat subduction regime, proposed to have begun at ~15-18 Ma (Gutscher et al., 2000; Jordan et al., 2001; Ramos and Folguera, 2009; Ramos et al., 2002; Yañez et al., 2001) and becoming completely flat at 29-30° S Lat (locally overturned, cf. Gans et al., 2011) between ~10-5 Ma (Gutscher et al., 2000; Kay et al., 1991; Kay and Mpodozis, 2002). From the study of borehole temperatures, Collo et al (2018) suggest that this region currently has a low geothermal gradient - below 20°C/km. Likewise, studies carried out in the Cenozoic strata associated with the flat subduction zone in the last decade show local and regional variations in the thermal regime, with gradients ranging between <20°C/km (Collo et al., 2011; 2015; 2018; Wunderlin et al., 2021) and 25-35°C/km (Stevens Goddard and Carrapa, 2018) for the Miocene. In this context, and despite their at least 7 km of thickness, there is a possibility that the Cretaceous to Cenozoic sequences in the Ischigualasto-Villa Union depocenter would not have generated sufficient burial for the older Permo-Triassic sequences to reach temperatures compatible with the oil and gas windows (between ~ 100-200°C cf. Tissot and Welte, 1984). An alternative hypothesis is that these temperatures could have been achieved during the Mesozoic, associated with a high heat flow regime.

The aim of this paper is to reconstruct the thermal evolution of the Ischigualasto-Villa Unión basin in the western Pampean Ranges of Argentina from Triassic to present-day in places affected by a multiphase deformation and where processes of flat-slab subduction are or have been active.

2. Geological setting

The Ischigualasto–Villa Union Basin is one of a numerous rift basins that developed on the western margin of southern South America during the Pangea pre-rupture extensional period between the Late Permian to Late Triassic (e.g. Uliana et al., 1989; Tankard et al., 1995; Franzese and Spalletti, 2001, Melchor 2007; Gulbranson et al., 2015). This basin is a NW–SE trending half-graben at least 120 km long and 50 km wide that has been modified by Neogene compressional tectonics associated with the development of the Andean foreland basin (Fig. 2A). In seismic cross-section, the Triassic strata display a wedge-shaped geometry (Rosello et al., 2005; Georgieff et al., 2009). The basal deposits of these Upper Permian-Triassic sequences overlap the Upper Paleozoic units of the underlying Paganzo Basin. The regional basal surface that marks the beginning of the subsidence in this half-graben is either erosive or non-erosive depending on the position in the basin. In the northern region, the Upper Permian-Triassic sequence is paraconcordant with respect to the underlying Permian deposits of the Paganzo basin (La Veteada Formation), while in the central and southern region of the basin, only the Pennsylvanian Guandacol Formation is preserved (at least 700 m of erosion, see Fig. 2B). The fill of the half-graben is represented by a 2500 m thick continental strata that comprises two major successions. The first is the thick latest Permian-early Triassic red bed succession, which includes the Talampaya and Tarjados formations (e.g., Milana and Alcober, 1994; Gulbranson et al., 2015). These units are covered by the Upper Triassic Agua de la Peña Group, which includes the Chañares, Ischichuca, Los Rastros, Ischigualasto and Los Colorados formations (e.g., Milana and Alcober, 1994; Melchor, 2007; Mancuso and Caselli, 2012). Milana and Alcober (1994) and Milana (1998) distinguished two rift episodes on the basis of seismic and tectonostratigraphic analysis. Basaltic flows and sills are interlayered in Triassic strata (Monetta et al 1993, Melchor 2007).

The Los Colorados Formation is unconformably overlain by the alluvial conglomerates and sandstones of the Cerro Rajado Formation (Bossi, 1977), which does not have fossil records or radiometric ages; it has tentatively been assigned by these authors to the Early Cretaceous. The Cerro Rajado Formation is unconformably overlying the Triassic sequences in the center of the half-graben, and instead shows a concordant relationship at the extreme north and south. Near the Cerro Rajado hill, an angular unconformity separates the Los Colorados Formation from Cenozoic sandstones (Malizia et al., 1995). The overlying Andean foreland basin record comprises 3.1 to 7 km of Neogene clastic sediments and is divided by a NNW–SSE trending basement high (the Valle Fértil Fault; Fig. 2A and B) into two depocenters: the Bermejo and Villa Union troughs (Rossello et al., 1996, 2005; Gimenez et al., 2000). The former has a maximum thickness of 7 km,

while the latter ranges between 3.1 and 7 km. The eastern margin of the Valle Fértil fault has been interpreted as a major transpressional left-lateral wrench zone forming a positive flower structure (Rossello et al., 2005), which inverted Triassic normal faults (Fig. 2A). The strata of the Ischigualasto–Villa Unión Basin are uplifted against the western (Valle Fértil fault) and eastern margin of the Ischigualasto - Villa Union intermontane Cenozoic depocenter (Fig. 2B). More than 7 km thick of neogene sediments in this depocenter are explained by the tectonic load and uplift of the Sierra de Famatina within the broken foreland (cf. Jordan et al., 2001) and the consequent provenance from this new source area to the east (Stevens Goddard et al 2020).

3. Methodology

Three detailed stratigraphic sections (north, east and south, Fig. 2B) were measured; these are considered as the most representative of the three-dimensional arrangement of the Triassic basin. These sections involved Upper Paleozoic, Triassic, Cretaceous and Cenozoic successions: (N) Ischichuca-Pagancillo creek in the northwestern sector; (E) Gualo river in the eastern-central part of the flexural margin; and (S) Ischigualasto National Park in the western-central part of the half-graben on the hanging-wall slope (Figs. 2A and 2B).

We present new coal petrography and vitrinite reflectance data of the Guandacol (Pennsylvannian), Ischichuca and Los Rastros Formations (Middle Triassic) and new analyses of clay mineralogy from all units in the three sections. Low-temperature thermochronometry using the fission tracks method in apatite (AFT) and the (U-Th)/He method in apatite (AHe) and zircon (ZHe) were conducted in selected samples from the northern and southern sections. Multi-method inverse thermal modelling of the data were conducted using the software QTqt (Gallagher 2012), aimed at delimiting the Partial Retention Zones for each thermochronometer and to investigate the thermal history, with a particular focus in documenting the age of the thermal peak and the time-temperature conditions attained during Cenozoic burial.

3.1. Coal petrography and vitrinite reflectance (%Ro)

Vitrinite derives from thermal transformation of woody tissues of vascular plants and their derived humic substances, which constitute the various huminite-vitrinite macerals and can be found dispersed in sediments (e.g., Stach et al., 1982; Teichmüller, 1987). Its optical properties are quite homogeneous and the transforming reactions are not reversible with exhumation and/or temperature decrease. Vitrinite reflectance is the most

widely used quantitative parameter to determine levels of thermal maturity in hydrocarbon exploration, as it is correlated with thermal evolution of host sediments, and provides consistent and reliable information on maximum burial depths (Lopatin, 1971; Stach et al., 1982; Tissot and Welte, 1984; Espitalie et al., 1985; Teichmüller, 1987; Sweeney and Burnham, 1990; Barker, 1996; Moore and Reynolds,1997; Hackley and Lewan, 2018, Burnham, 2019). A total of 46 samples from the three columns were analyzed petrographically (Fig. 3, Table 1 and supplementary material 1a,b,c). Sample preparation followed procedures outlined in ASTM D2797/D2797M-11a (ASTM, 2011). Vitrinite and inertinite maceral identification follows recommendations outlined by the International Commission for Coal and Organic Petrography (ICCP) for vitrinite (ICCP, 1998), inertinite (ICCP, 2001) and Pickel et al. (2017) for liptinite macerals. Vitrinite random reflectance was performed on 29 samples according to ASTM D7708-14 (ASTM, 2014). On each sample, from about 10 to 110 measurements were carried out on well-preserved or slightly fractured vitrinite. Measurements were carried out at INCAR (Oviedo Spain) and Geolabsur (Buenos Aires, Argentina).

3.2. Clay mineralogy and I/S characterization

The characterization of illite/smectite (I/S) interlayer phases present in clastic sequences is a very useful and widely used tool to approximate thermal trajectories in sedimentary basins, since a prograde transformation takes place with increasing temperature, in which the illite content in the I/S and the I/S ordering type (Meunier, 2005) increases progressively. A total of 71 samples from the three sections were analyzed (22 samples from the northern section, 43 samples from the southern section, 6 samples from the eastern section). Separation of <2 microns clay minerals fraction was carried out following the recommendations of Moore and Reynolds (1997). The mineralogy of the different fractions was determined through X-ray difractometry (XRD) analyses in oriented samples, between 4 and 35 º2q, with a step size 0.02 º2q and a scanning time per step of 35 s. The mineralogical identification of the clay fraction was conducted according to the positions of the basal reflections of air-dried (AD), ethylene-glycol solvated (EG), and heated to 500ºC for 4 h (C) XRD patterns, according to Moore and Reynolds (1997). For the I/S characterization (evolution of I/S with depth) the illite proportions in the I/S were established for all samples in each of the sections following the method of Moore and Reynolds (1997).

3.3. Thermochronology

Apatite fission-track (AFT) and U- Th/He Methods

Thermochronology deals with the reconstruction of the thermal history of rocks based on the quantification of the products of radioactive decay accumulated in minerals through time. (Dodson, 1973; Reiners, 2005). The closure temperature is defined as the approximate temperature at which the loss of the radiogenic product is much slower than their production, leading to their effective accumulation within the mineral lattice. It is well established that the closure temperature varies with cooling rates, mineral kinetic variability, and other conditions intrinsic to each system (e.g., Ehlers & Farley, 2003). Slowly cooled samples residing at partial retention temperatures for long periods exhibit more age dispersion (e.g., Barbarand et al., 2003; Shuster et al., 2006).

The AFT method is based on the quantification of damage to the crystal (i.e., fission tracks) that results from the spontaneous fission of ^{238}U. Fission tracks are ~16 microns long when formed; at temperatures above ~60°C, they progressively shorten until fully annealing at temperatures of ~120 °C for geologic times (>10e6 years). This interval is known as the partial annealing zone (PAZ, Wagner et al., 1989). Due to their thermal instability, the track length distributions and the mean track length (MTL) can be used as proxies to quantify the amount of annealing experienced by the apatite crystal (Green et al., 1985) and therefore investigate their thermal history. The C- axis parallel length of the etch pit (Dpar) can be used as a proxy to quantify resistance to annealing for individual crystals, a necessary condition for thermal modeling (Barbarand et al., 2003; Carlson et al., 1999; Ketcham et al., 1999). The grinding and concentration of heavy minerals were carried out in the Heavy Minerals Grinding and Concentration laboratory of CICTERRA and in the Low Temperature Thermochronology Laboratory of the University of São Paulo. Two aliquots of each sample were prepared. One aliquot was analyzed for age determination by the External Detector Method (Gleadow and Duddy, 1981), using an Olympus BX51 microscope with a digitizing tablet and the FTStage 4.05 software (Dumitru, 1993) at the Low-Temperature Thermochronology Laboratory of the University of São Paulo. Ages and errors were calculated using the zeta calibration method (Hurford and Green, 1983), using zeta calibration factors of 74.5 ± 4.0 and 80.2 ± 2.1 n cm2 tr-1 y-1 (CN1 glass; Cecilia Wunderlin) obtained by analyzing a total of 9 Durango and Fish Canyon Tuff age standards along two analytical sessions. An uncertainty of 1σ is reported for all ages. The other aliquot was irradiated with ^{252}Cf fission-fragments at the University of Texas at Austin in order to make visible a greater number of confined tracks for length measurements (tables SM2a in supplementary material). The AFT analysis was performed on an average of 20 grains per sample (see Table 3 and tables SM2a and radial plots SM2b in supplementary material) in 9

sandstone samples retrieved from two sections. The samples were collected from the Pennsylvannian, Triassic and Cretaceous to Cenozoic sequences and are separated from each other by approximately 300-500 m (stratigraphic thickness). The potential effects of variations in track annealing kinetics were evaluated by measuring Dpar values.

(U- Th- Sm)/He thermochronology is based on the production and accumulation of radiogenic ^{4}He that results from the alpha decay of U, Th, and Sm. Crystal size, mineral composition and, specially, radiation damage associated with alpha recoil and nuclear fission control the closure temperatures for different minerals (see Ault et al., 2019 for a review). For apatite, the method provides information on the thermal history between 40 and ~80 °C (apatite partial retention zone or APRZ, Farley, 2002), and in unusual conditions up to 120 °C (Flowers et al., 2009, Gautheron et al., 2009), whereas zircon U- Th/He thermochronology provides thermal history information between 140 and 220 °C (zircon partial retention zone or ZPRZ, Guenthner et al., 2013). Apatite and zircon inspection and grain selection was performed at the Low- Temperature Thermochronology Laboratory of the University of São Paulo. Each apatite or zircon grain was photographed and packed in 1 mm Pt or Nb tubes, respectively, using an Olympus SZX16 stereoscopic microscope, following the procedure proposed by Farley (2002). The grain dimensions and the number of crystal terminations were determined to calculate the correction factor associated with alpha ejection (Ft, Farley et al., 1996). Helium measurements were performed at the University of Potsdam, Germany. The Pt and Nb tubes were loaded into a 25-hole sample chamber of an ASI Alphachron He analysis and extraction system, equipped with a 978nm 30W coherent diode laser and a Pfeiffer Prisma 200 Quadrupole mass spectrometer. The abundance of 4He in the purified gas was measured by isotope dilution using a 3He tracer, calibrated against a gauged 4He standard. A second analysis or re-extraction was performed for each sample to ensure that the grain was completely degassed. Following degassing, the concentrations of U, Th and Sm were measured at the GFZ Potsdam by isotope dilution using a Thermo Element 2 XR ICP-MS equipped with a CETAC ASX-520 automatic sampling system that was run in the low resolution to maximize ion transmission. Additional methodological details are provided in Zhou et al. (2017) and Galetto et al. (in press), for apatite and zircon, respectively. Age calculation followed the procedures of Meesters and Dunai (2005). An uncertainty of 2σ is reported for all ages. The potential effect of radiation damage on the AHe and ZHe data was evaluated by comparing the effective uranium (e[U] = U + 0.235 * Th) and the grain size with individual ages (see SM3) as a proxy for radiation damage, following the model by Flowers et al. (2009).

Multi-method thermochronological modeling

Inverse thermal modeling was applied in samples with data from more than one thermochronometric system, including AHe, AFT, and ZHe data, as well as Ro data from interbedded mudstones.. Samples were modeled using the QTQt v5.7.0R software (Gallagher, 2012), which allows probable thermal histories to be extracted using Bayesian transdimensional statistics. At least 200,000 iterations were performed and we based our interpretation on the expected model obtained. The expected model is a weighted mean model, where the weighting is provided by the posterior probability for each model (Gallagher, 2012), and lies between the maximum likelihood model (more complex) and the maximum posterior model (less complex). We used the kinetic model of Ketcham et al. (2007) for the fission track annealing parameters and the radiation damage model of Flowers et al. (2009) for the AHe system. The basin %Ro model of Nielsen (2017) was used for the kinetics of vitrinite reflectance. A second set of models was run using a multi-sample approach, in which samples from the same stratigraphic section were modeled together.

Taking into account the geological configuration of the modeled samples, we applied restrictions to the model based on geological information that includes the depositional age of each level, the depositional (20 ± 5 °C) and current (20 ± 5 °C) temperatures, and near-surface (i.e., 20-40°C) residence anytime between 100 and 70 Ma, which is required by the presence of an unconformity. In addition, modeling of partially reset samples was allowed by adding a constraint at sufficiently high temperatures (280-300°C) way before sediment accumulation (500-480 Ma).

3.4 1D thermal modeling

Simplified reconstructions of the burial and thermal history of the late Permian-Triassic successions have been performed using the software package 1D-Petromod®. This software simulates the thermal history by considering the effects of sediment accumulation, pore pressure changes, compaction, and basal heat flow. In addition, by using kinetic information of organic matter transformation it allows,, modeling of hydrocarbon generation (Schlumberger 2011). In this case, the main assumptions for modeling are that: (1) because it is an entirely siliciclastic section, rock decompaction factors apply only to clastic deposits, according to Sclater and Christie's method (1980); (2) seawater depth variations are ignored because all deposits involved in this study are continental and the thermal evolution is mainly affected by sediment thickness rather

than by water depth; (3) a surface temperature of 20°C is assumed and (4) variable heat flow values through time are assumed.

A 1D model was aimed to obtain the heat flow values that would have been necessary in each period to reach the maximum defined temperatures. Thicknesses and ages of stratigraphic units have been derived from this work and previous papers (eg. Malizia et al. 1995; Melchor 2007). Burial and thermal models were constrained by organic and inorganic thermal indicators. Illite content in mixed layers I-S was converted into Ro eq% values using the correlations between these two indicators (Aldega et al., 2007; Merriman and Frey, 1999).

4. Results

4.1. Organic matter maturity

The Guandacol, Ischichuca and Los Rastros Formations are the only units with carbonaceous shales from which this analysis could be carried out successfully. The Ischigualasto Formation has thin and scarce levels with low content of organic matter; these were analyzed but were barren.

The vitrinite reflectance values (% Ro, n=29) are shown in Table 1 and Fig. 3. The individual measurements of each sample and its corresponding statistical analysis are in the supplementary material 1. The %Ro values obtained for organic matter in the Pennsylvanian Guandacol Formation range between 1.00% and 1.12%, compatible with the late oil to wet gas window. The Ischichuca and Los Rastros Formations in the northern section show values within a range of 0.75 to 0.90 %Ro. These formations have slightly lower values in the southern section (between 0.53 and 0.82%Ro). It is necessary to highlight that in this last section it was possible to sample carbonaceous levels that are in higher stratigraphic positions within the Los Rastros Formation. Substantially lower values were measured in the eastern section (between 0.75 and 0.43% Ro), which correspond to values below the oil window.

4.2. Clay mineralogy and I/S characterization

I/S ordering type, illite% content in I/S and clay mineral fraction composition from psamopelitic samples (n=71) from the three studied sections are shown in table 2 and Fig. 3.

In the northern section, Cenozoic and Cretaceous units show a domain of illite/mica and I/S, with minor chlorite contents and traces of corrensite. Within the Triassic sequences, the Los Colorados and Ischigualasto Fms samples are composed of illite/mica and I/S, with minor kaolinite in some samples from the Ischigualasto Fm, while the Ischichuca Fm show illite/mica, I/S, chlorite and kaolinite in almost all the samples. Cenozoic and Cretaceous samples record R0 I/S ordering type, with 5-30 illite% in I/S. With the exception of one sample from the Los Colorados Fm., Triassic samples present R1 and R3 orderings with 65-85 illite% , showing an increase of illite% content from top to base and an abrupt change from<5 to 65 illite% between the Cerro Rajado and Los Colorados Formations (Fig. 3).

In the southern section, Cenozoic samples show a domain of illite/mica and I/S, with minor proportions of chlorite and traces of corrensite and kaolinite in a few samples. Triassic units show a domain of illite, kaolinite and I/S, with traces of chlorite in some samples. Samples from the Pennsylvannian Guandacol Formation show a domain of illite and chlorite, traces of kaolinite and an almost lack of I/S. R0 I/S ordering type with <10 to 25 illite% in I/S was identified in Cenozoic samples. Triassic samples present mainly R1 to R3 orderings, with 55 to 85 illite% in I/S, showing, as in the northern section, an increase of illite% content from top to base and an abrupt change (<10 to 65 illite%) between the Río Mañero and Los Colorados Formations (see red circle in Fig 3). The Ischigualasto Formation shows an exception in this trend, with presence of smectite and absence of I/S in all the analyzed samples.

Within the eastern section, the Ischichuca Formation was analyzed. All the samples show illite/mica, I/S and kaolinite coexistence, with R0 ordering types and 20-50 illite% contents, values substantially lower than those obtained for this unit in the northern and southern sections.

4.3. Thermochronology

Eight sandstone layers were sampled in the northern section and six in the southern section. Good apatite yields were obtained in a total of nine samples . The sample locations within the stratigraphy are shown in Fig. 3 and analytical results are displayed in Tables 3 and 4, Figs. 4 and 5, and SM2a. In order to provide a more meaningful regional assessment of the thermal patterns of the basin, we integrate our new data with 2 published AFT, 2 AHe, and 1 ZHe ages (Fosdick et al., 2015; Ortiz et al., 2015, Tables SM2a).

4.3.1. Apatite fission-track ages

As was mentioned before, nine samples from the northern and southern sections were analyzed using the AFT method. Two samples from the Pennsylvanian Guandacol Formation (N-051 and S-172) yielded Miocene central ages of 9.3 ± 1.5 and 8.6 ± 1.6 Ma (Table 3, Fig. 3). Only a few tracks were available for length measurements in sample S-172 (N=2) and yielded a mean of 12.24 ± 0.07 μm (Fig. 4). Dpar values vary from 1.63 μm to 1.76 μm. Six samples were analysed from the Triassic sequences (N-148, N-145, N-005B, S-IJ1, S-163, S-167) and yielded central ages between 56.3 ± 15.8 Ma and 137.1 ± 18.9 Ma. Three of these samples with varying numbers of lengths are characterized by reduced tracks (between 11.18 ± 0.27 μm (n=101) and 12.52 ± 0.53μm (n=7)). Furthermore, the track lengths of N-145, N-148 and S-163 are unimodally distributed (Fig. 4). Dpar values of these six samples range between 1.66 μm and 1.99 μm (Table 3). The sample attributed to the Cretaceous Cerro Rajado Formation, in the northern section (N-150), yields a central AFT age of 67.4 ± 9.8 Ma and the shortest mean track length, of 10.70 ± 0.28 μm (n=61), with an unimodal distribution (Fig. 4). The Dpar value of this sample is 1.76 μm.

A unimodal track-length distribution, $P(\chi^2)$ values <5%, and the relationship between the obtained ages and the time of deposition for all Mesozoic samples suggest that the AFT ages are reset or partially reset. On the contrary, the Miocene ages of both Pennsylvanian samples (N-051, S-172) are interpreted as fully reset, despite the $P(\chi^2)$ values of 0%. The discordant ages could arise from differences in annealing kinetics, but they are not characterized by the Dpar, as there is no correlation of ages with Dpar values. A concordant fully reset AFT age of 5.8 ± 0.8 Ma in a sample from the Guandacol Formation from the same section is reported by Fosdick et al (2015, Tables SM2)

4.3.2 Apatite (U-Th)/He ages

Twenty-two aliquots from five samples were analysed using the AHe method and yielded Ft-corrected ages between 1.9 ± 0.3 and 43.6 ± 0.8 Ma (Table 4), with ages older than 10 Ma only present in the younger (Triassic) samples form the northern section. Single-grain AHe ages in every sample are younger than both the corresponding AFT age and the depositional ages (Fig. 5), suggesting either total or partial resetting of the AHe system after sediment accumulation. The analyzed apatite grains have an equivalent

spherical radius between 28.6 and 107.5 μm and eU contents between 4.8 and 86 ppm (Table 4).

Intra-sample dispersion decreases for older, deeper buried samples, so that only the Upper Triassic samples N145 and N148 from Los Colorados Formation include aliquots older than 10 Ma, and only the stratigraphically younger of them (N148) two aliquots older than 20 Ma. At least part of the dispersion can be attributed to grain sizes for sample N148, with older ages for larger aliquots or, in the case of sample N145, to radiation damage effects, with older ages in eU-richer samples (Fig. SM3). Finally, the stratigraphically shallowest sample N150, from the Cretaceous Cerro Rajado Formation, yielded moderately dispersed ages younger than 10 Ma. As shown below, we attribute such a dispersion to partial resetting in a detrital sample made up of apatites with dissimilar radiation damage that is not captured by eU contents. In contrast, the stratigraphically deepest sample in the northern profile, N051, from the Pennsylvannian Guandacol Formation, as well as the Triassic Ischichusca Formation sample S-167 from the southern profile yielded reproducible ages with weighted mean values of 2.9 ± 0.1 and 4.5 ± 0.4 Ma, which suggest full resetting of the AHe system.

These young and reproducible AHe ages in the southern section are compatible with the ages obtained in one Triassic (SVF11, 2 aliquots, weighted mean of 2.2 ± 0.1 Ma) and two Pennsylvannian samples (SVF01, 2 aliquots, 4.9 ± 1.1 Ma; SVF02, 4 aliquots, 4.0 ± 0.5 Ma) in the same section by Fosdick et al., (2015) and Ortiz et al., (2015) (Tables SM2)

4.3.3 Zircon (U-Th)/He ages

ZHe data from two aliquots of sample S-172 from the Pennsylvannian Guandacol Formation were obtained during this study and show ages of 314.0 ± 4.1 Ma and 281.5 ± 4.6 Ma. There is a positive correlation with both grain sizes and eU contents (Fig. SM3). Similar stratigraphic levels within this Pennsylvannian strata sampled by Fosdick et al. (2015) yielded similar ages of 197-259 Ma (SVF-01, Table SM2, Fig. 5), with a positive correlation with eU (SM3). As ZHe ages from the Guandacol Formation are either younger (SVF-01) than the depositional age, or similar and older (S-172) than deposition (Fig. 5), they suggest that temperatures during burial were sufficiently high for partial resetting of the system, perhaps close to the temperature limit for total resetting.

4.4 Thermal modeling

4.4.1 Individual thermal models

We performed inverse thermal modeling in those samples with data from more than one thermochronometer and with either a fair amount (31-102) of track-length measurements, or available vitrinite reflectance data from adjacent mudstones. Four Triassic samples from the Ischigualasto-Villa Union Basin (N150, N148, N145, S167) met those conditions and were modelled to extract their thermal histories (Fig. 6 and 7, Table SM2). The input data for the modelling were the AFT ages, track-lengths, and Dpar data, the AHe single grain ages of all aliquots, given that age dispersion could be explained by either grain size or radiation damage, and Ro% data. A summary of data used for each model is presented in Table S3.

Boundary conditions were imposed on each thermal model in order to obtain geologically reasonable cooling histories: 1) the starting-point of the modelled time temperature path is given at a sufficiently high temperature (280-300°C) before sediment accumulation (480-500 Ma), which represents the time-temperature trajectories associated with the Paleozoic provenance for Triassic samples(Melchor 2007); 2) residence at surface temperatures of 20 ±10 °C during Triassic sediment accumulation; 3) near-surface residence (20-40 °C) during Cretaceous, associated with deposition of the unconformably overlying Cerro Rajado Formation, and 4) present-day temperatures of 20 ± 10 °C.

For the Triassic samples (N-145, N-148 and S-167) the obtained thermal histories suggest that the thermal peak was attained during Mesozoic times and was followed by a Late Cretaceous-Cenozoic heating of lesser magnitude until the onset of cooling in Miocene-Pliocene times (Figure 4). The more probable age for the peak temperatures during the early thermal event is shown in the models of samples N148 and N145 and correspond to the Late Triassic-Jurassic (210-150 Ma). A most likely maximum temperature of ~160°C during these peak events is obtained for sample S167, due to the inclusion of Ro% data in the modeling (Fig 4H), and is compatible with full resetting of the AFT and AHe systems. The peak temperature conditions during the second heating event range between 70-75°C for the Cretaceous and Triassic rocks in the northern section, and 80-85°C for the Triassic rocks in the southern section (Figure 6). These results are compatible with partial resetting of the AFT system, and partial to total resetting of the AHe system. The age for the onset of this more recent cooling ranges from 15 to 4 Ma.

Despite their relevance for reconstructing the thermal histories, the results of thermal modeling of individual samples illustrate the intersample dispersion inherent to the

approach, especially in the age for onset of Cenozoic cooling. In order to overcome this shortcoming, we conducted multi-sample thermal modeling.

.

4.4.2 Multi-sample thermal modelling

We ran multi-sample modeling on two stratigraphic profiles, including paleothermometric (Ro%) and thermochronologic (AHe, AFT and ZHe) information of new and published Pennsylvannian, Triassic and Cretaceous samples using the QTQt software (Gallagher, 2012). For the northern profile, we used data from 5 samples covering ~3.4 km of stratigraphic thickness, which comprise AHe data of 4 samples (18 aliquots), 4 AFT ages, track-lengths of 3 samples (n= 31, 61 and 102) and vitrinite reflectance from sample N43. For the southern profile, 7 samples encompassing 1.3 km of section were modeled, including AHe data from 4 samples (12 aliquots), 5 AFT ages and track-length data from 2 samples (n=7 and 2), ZHe data from 2 samples (5 aliquots), and Ro% data from 6 samples. In a first modeling run, the boundary conditions and additional geological constraints imposed for modeling constraints were the same as for individual sample models, as described in section 4.4.1. A second modeling run was designed to include the most likely age of thermal maximum at the Triassic-Jurassic boundary (210-180 Ma). A summary of data used for multi-sample modeling is shown in Table S3.

The results of multi-sample modeling are consistent with the presence of a Mesozoic heating event in which the highest temperatures were achieved and a subsequent Cenozoic heating event with a lower thermal peak (Fig. 7 and 8). During the first event, the unconstrained models show peak conditions for the deepest, Pennsylvanian, samples in both profiles, at a similar temperature of ~160°C, but with striking different maximum burial ages, Late Permian (~255 Ma) in the southern profile and early Cretaceous (~110 Ma) in the northern profile. Such conditions, despite being compatible with full resetting of the AHe and AFT systems but partial resetting of the ZHe system, and with the observed Ro% values of ~1.1%, are difficult to reconcile into a coherent single thermal history for localities 35 km apart in the basin. In the second event, peak thermal conditions would have been achieved at similar times of 10-6 Ma, but with hotter temperatures in the south (140°C) than in the north (90°C). Both models readily reproduce the observed reset thermochronometric ages, AFT lengths and Ro% data. However, the dissimilar pattern of ages of the first thermal peak and of temperatures in

the second thermal peak for localities situated 35 km apart suggests that these unconstrained models hardly represent a reliable history.

Motivated in the results of individual sample models, the presence of basaltic flows and sills interlayered in Triassic strata (eg. Milana and Alcober 1994; Monetta et al 1993, Melchor 2007), and previous thermochronological studies in the region (Enkelmann et al. 2014, Bense et al. 2014, Ortiz et al. 2021) a second set of multi-sample models employed an additional constraint of residence at up to 200°C in the latest Triassic-earliest Jurassic (210-180 Ma). The expected models (Fig. 8) significantly improve the model fit with respect to the observed data in the southern profile (Loglikelihood (LL) of -446 vs -994 for the unconstrained model) and present a similar fit in the northern profile (LL of -1521 vs 1421). Maximum temperatures for Pensylvanian samples of ~160°C at the late Triassic (210-200 Ma) and anytime between 210-100 Ma in the southern and northern profiles, respectively, characterize the first thermal event. Heating above 120°C of the upper Triassic samples would only have occured in the southern profile (see thin gray lines in Fig. 8, left panel). In the Cenozoic thermal peak, maximum temperatures close to 100°C for the Pennsylvanian samples in both profiles were attained before the onset of final cooling at 7-9 Ma (See Fig. 8, inset). The top sample in the northern Profile (Cerro Rajado Formation) attained ~60°C in this latter event, in agreement with full resetting of AHe ages for less-retentive apatites and partial resetting of retentive apatites, as well as with partial resetting of the AFT system. Interestingly, a Cenozoic decrease in the thermal gradient (i.e., a decrease in the separation between the red and blue curves in Figure 8) is suggested in both profiles. The subordinated increase in this gradient shown by the local increase in the separation of the t-T paths of the bottom and top samples (i.e., cooling of the top sample accompanying heating of the bottom sample) could correspond to a thermal blanketing effect (e.g., Wangen et al., 1995)

5. Discussion

The multi-proxy approach of this study delineates the thermo-temporal evolution of the Triassic Ischigualasto basin. At first, we used % Ro and clay minerals analysis to estimate the maximum temperatures reached by different rock units, theirlateral variations and thermal “discordances” are inferred. Then, by adding thermochronological and 1D thermal modeling, a refined t-T evolution is proposed.

5.1. Maximum temperatures and lateral variations

For the northern and southern sections, the %Ro analysis suggests that the maximum temperatures reached by the Pennsylvanian sequences did not exceed 170 °C (Guandacol Fm; cf. Sweeney and Burnham, 1990; Nielsen et al., 2015; Burnham, 2019) and upper Triassic intervals did not exceed 130 °C (Ischichuca and Los Rastros Fms, Fig. 9A).

Clay mineral associations identified along these western sections (northern and southern sections) show an increase in the prograde reactions, with illitization of smectite, from the top to the base. This is particularly recognisable by the changes in the interlayered I/S, from poorly ordered (R0), with illite contents not exceeding 20% in the Cretaceous-Cenozoic Cerro Rajado and Rio Mañero formations, to R1 type arrangements, with contents of illite between 65 and 80%, in the Triassic Ischigualasto and Los Colorados Formations, and R1 and R3 orderings, with up to 85% of content of illite, towards the base of the lower Triassic Ischichuca Formation. These results are consistent with the variations in the % Ro values (Fig. 3).

Considering both the % Ro and illite % in I/S values obtained for Ischichuca and Los Rastros Formations in the western region of the basin, maximum temperatures ranged from 110 to 140 ºC (cf. Bird et al., 1999; Srodon, 2007, see Fig. 3 and Fig. 9A). On the other hand, for the Los Colorados and Ischigualasto Formations, where the % Ro analysis was not available due to the absence of organic matter-rich levels, temperatures of ~ 100 °C can be estimated based on the I/S present (cf. Burnham and Sweeney, 1989; Merriman y Peacor, 1999; Merriman y Frey, 1999, Burnham, 2019, Fig. 9A).

East-west variations are recorded in both the% Ro and clay minerals associations, indicating a gradual heating to the west (Fig. 9A). For the Ischichuca and Los Rastros formation, Illite% in I/S between 20 and 50% (R0) were recorded in the Rio Gualo section, while Illite% in I/S between 75 and 85% (R1-R3) are recorded in the western sections. These results are consistent with those obtained by Mancuso et al. (2020) for the Tarjados and Los Rastros Formations in the Río Gualo section, which show an increase in illite content in I/S with depth, reaching R0 ordering type (15% illite) at the base of the Los Rastros Fm. Temperatures between 80 °C and ~100 °C are inferred for the Ischichuca Formation based on our % Ro results (Fig. 9A).

5.2 Pre-Cenozoic heating

I/S and %Ro data together suggest that the maximum thermal peak is not related to Cenozoic sedimentation. In the northern and southern sections, an abrupt discontinuity

in the illite % in I/S and the ordering types was identified between the Cretaceous-Cenozoic successions and the underlying Triassic units (Fig. 3), marked by a total absence of interlayered type R1 in the former (inferring that the R3 ordering type present is detrital), and the abrupt appearance of coexistent R1 and R3 types in the latter. This interpretation is clearly supported by the different individual thermochronological models as well by the multi-sample analysis, which shows that maximum temperatures were reached during the Mesozoic, prior to the deposition of the overlying units. In addition to I/S, %Ro and inverse multi-method thermochronometric models, data from other samples available from literature (Ortiz et al., 2015; Fosdick et al, 2015) support our interpretation. Partially reset ZHe ages in our S-172 sample and of SVF 001 sample from Fosdick et al. (2015), and Ro values of ~1.1% show that Pennsylvanian sediments reached maximum temperatures of ~160°C. Inverse models that combine all information and geological constraints demonstrate that this thermal maximum was attained during the Triassic (Fig. 9A). After this maximum temperature peak, the Guandacol Formation would have experienced slow cooling, and resided in the AFT PRZ (120-60 °C) until the Miocene (Fig. 8, Table S3). This is compatible with two rifting phases that affected the Sierras Pampeanas, the older of which took place in the Triassic and was more intense than a subsequent Cretaceous event (Ramos, 1999).

Regional thermochronological data supports an interpretation of a main Triassic heating event. In the Sierra de Chepes (150 km SE), the Pennsylvanian and Permian sequences overlie the Ordovician basement and there is no sedimentary record for the Triassic. There, Enkelman et al., (2014) report apatite ages of the basement samples and the overlying Upper Paleozoic strata that are younger than their depositional ages (AFT: 259-225 Ma and apatite (U-Th)/He: 175-142 Ma). They suggested maximum heating during Permian and Triassic times at temperatures in the lower part of the apatite partial annealing zone, probably between 80 and 140°C, followed by cooling associated with basin inversion, uplift and exhumation of Sierra de Chepes during the Late Triassic. This occurred concomitantly with the formation of the Ischigualasto Basin. Enkelman et al., (2014) suggest a combination of basement burial by Upper Paleozoic strata (<1000m) and a very important increase in the geothermal gradient during Permian and Triassic times as the probable reasons for the heating of the basement rocks. These authors also suggest a long-lasting very slow cooling trend from the latest Jurassic through Cretaceous time, indicated by the wide spread in the bedrock AHe ages (244–142 Ma). Recently published single-sample thermal modeling of AFT and AHe data from Ordovician plutonic and Triassic sedimentary rocks collected in the Sierra de Valle Fértil, 10 to 50 km to the south of our study area have been used to infer discrete periods of

Mesozoic heating followed by Cretaceous and Cenozoic cooling (Ortiz et al. 2021). As no Cenozoic basins are preserved in the Sierra the Valle Fértil, thermal trajectories without Miocene burial were able to reproduce the observed thermochronometric data. This is consistent with post Triassic-rifting thermal relaxation. Likewise, petrography and geochemistry (trace elements and REEs) of Triassic basalts in the adjacent Sierra de Valle Fértil suggest an origin by partial melting of an asthenospheric mantle in the presence of garnet, and would indicate that the melt that originated these basanites and alkaline basalts did not have components derived from subduction and / or cortical contamination (López et al. 2020). This is compatible with a thinned crust and high regional geothermal gradient. More recently, Triassic heating with strong along-strike gradients has been demonstrated by single-sample and multi-sample inverse modeling of AFT, AHe and ZHe data in the eastern Sierras Pampeanas (Martina et al. 2021). These authors suggest a major regional hiatus of ~150 m.y. that coincides with a period of protracted Triassic heating following Carboniferous cooling and exhumation. According to these authors, the lack of sedimentary basins indicates that reheating cannot be related to burial. Martina et al. (2021) mentioned that basalt thermobarometry suggests “normal” mantle potential temperatures and an asthenospheric window associated with ridge subduction as a potential mechanism for Triassic heating.

Based on all the considerations mentioned above, we suggest that the maximum temperatures would have been experienced during the Triassic (Fig. 9A). If this was the case, it is unlikely that maximum temperatures were reached due to burial within a normal thermal regime. According to the different paleothermal models for normal thermal regime, at least ~1500 meters of unroofing associated with the Triassic-Cretaceous unconformity would have been necessary to reach the identified % Ro and % Illite in the I/S values (cf. Merriman and Peacor, 1999; Merriman and Frey, 1999). Moreover, considering the paraconformable character attesting to the low erosive capacity of the discordance at the base of the Cretaceous sequence, as well as absence of such thickness in any other part of the region, it is unlikely that major erosion has taken place. Peak temperatures of ~ 95°C recorded at the top of the Triassic sequences (sample N-148, Fig. 8) in the northern section suggests that these units would have reached these temperatures even at levels close to the Triassic paleosurface (in the order of hundreds of meters). Peak Triassic temperatures are suggested by inverse multi-method thermal modelling (Fig. 7 and 8). In the southern profile, where our data best captures the Triassic thermal patterns, there is a modeled difference of ~70° C between the top and the bottom samples (SJ1, ~100°C ±10°C; SVF01, 170°C ±10°C, respectively). With an actual stratigraphic separation of 1.3 km between samples, and a

conservative 30% addition due to post Triassic compaction, a geothermal gradient of 40-50°C is obtained (assuming no material was eroded due to the low to zero erosive capacity of the overlapping unit, see 2.Geological Setting).

Peak temperatures in the northern and southern sections (Ro% 1.14, ~170°C), which are close to the main normal fault of the Triassic half-graben, (rapidly decreased 40 km towards the east (Ro% 0.8., ~140°C). Such abrupt lateral thermal variations have been documented with thermochronometry in extensional basins (e.g., Fitzgerald et al., 1991, 1994; Ehlers and Chapman, 1999; Stockli et al., 2000, 2002; Stockli, 2005; Carrapa et al., 2014). Asymmetric subsidence across half grabens can account for greater burial, and hence heating, along the sectors of the hanging-wall located closer to the principal normal fault (Ring et al., 1999; Reiners and Brandon, 2006, Ortiz et al. 2021). A possible complementary interpretation for this thermal asymmetry of the Triassic basin is to consider that the main heat source would have been the principal normal fault of the half-graben (Sierra de Valle Fértil Fault), which likely behaved as the most active zone for the rise of heat. This is compatible with the profuse bimodal volcanism throughout the entire Triassic column in the northern and southern sections (eg. Moneta et al., 1993; Milana and Alcober, 1994; López et al. 2020), and with the conductive heat transfer model developed by Makhous and Galushkin (2005). Based on the initial thermal state of a continental rift, Makhous and Galushkin (2005) postulate that the lithosphere was affected by a decrease in heat flow ~10 km away from the main fault during the first million years of its activity, and with a longer time stabilization of the thermal field ~90 km away (in the order of tens of millions of years), producing a redistribution in the isotherms from the base of the lithosphere.

5.3 Low geothermal gradient during Cenozoic subsidence and Miocene exhumation

Inverse thermal modeling results show that despite the thick Cenozoic succession accumulated in the region (~7000 m, cf. Rossello et al 2005, Georgieff et al 2009, Canelo et al., in press), the highest temperatures in the Triassic successions would have been reached during a pre-Cenozoic thermal stage. Miocene AFT ages, suggesting a complete reset of the system during the Cenozoic burial, only occur in Pennsylvanian units. Noteworthy, Triassic sample S167 corresponds to a horizon where Ro% data ranges between 0.7-0.8% (T = 125-140°C), yet its AFT is 68.3 ± 11.6 Ma. Therefore, the peak temperatures of > 120°C °C recorded in the Triassic and Pennsylvannian units would have been reached prior to the Cenozoic at a depth of up to ~3000 m. The lack of

Cenozoic resetting of the ZHe and AFT systems in the Triassic sequences in spite of the increase in sedimentary thickness and, consequently, in the burial depth during the Cenozoic, is likely related to a strong decrease in the thermal regime, compatible with the low regional gradients proposed for this interval associated with Cenozoic flat-slab subduction (Collo et al., 2011, 2015; Fig. 9B). Interestingly, the multi-sample thermal model of the northern section (Fig. 7) captures such a decrease in heat flow. While the uppermost sample of the profile (N150) exhibits slow Cenozoic cooling before the rapid final late Miocene to recent cooling episode, the bottom sample (N051) underwent slow heating. Either a combination of burial and decrease in the heat flow, or thermal blanketing associated with the deposition of cold sediments (cf. Wagen, 1995), are required to explain such a divergence in the t-T paths associated with burial.

According to thermochronological models, cooling of the entire sections would have started at 7-9 Ma (Fig. 8), concomitant to sediment accumulation of the upper Miocene strata (Malizia et al., 1995, Fig. 9B). It should be noted that at least in the northern section of this work, sedimentation continued until the Pliocene (cf. Lemos Santos et al. 2018, Canelo et al., in press). In this context, cooling of the involved units could be associated with the variation in the thermal flux in the region, as it has been documented based on borehole, seismic, thermochronological and magnetic data, as a consequence of the initiation of a flat subduction regime from approximately 15 Ma (Gutscher et al., 2000; Gutscher and Peacock, 2003; English et al. 2003; Alvarez et al. 2014; Marot et al., 2014; Collo et al., 2018; Sanchez Nassif et al. 2019; Sanchez Nassif et al 2021, Fig. 9B). Such is the case of the Cenozoic sequences 100 km farther to the north in the Vinchina depocenter (Collo et al., 2015), and also to the west in the Bermejo depocenter (Dávila and Carter 2013; Richardson et al. 2013; Hoke et al. 2014; Bense et al. 2013; Collo et al. 2018; Wunderlin et al., 2021), as well as with those recorded for other flat slab regions (eg. Dumitru, 1990, Dumitru et al., 1991, Gutscher 2002, Manea and Manea 2011). This complex thermal evolution, in which maximum temperatures and cooling episodes are not directly associated with maximum burial and exhumation events, respectively, has already been recorded in other Precordilleran basins affected by the flat slab (Wunderlin et al., 2021). Moreover, Ortiz et al. (2021) identified three cooling pulses in basement samples from the Sierra de Valle Fértil immediately south of the Ischigualasto Basin, and associated them with exhumation stages during the Paleogene, middle Miocene and Mio-Pliocene, respectively. These authors suggest that greater relief was produced - and eroded - during the Mio-Pliocene indicating greater fault displacement during the final cooling phase. Consequently, the influence of exhumation processes on cooling, at least partially, cannot be ruled out.

5.4 Thermal history model (Petromod)

As was mentioned above, the definition of two clearly differentiated thermal episodes allows interpreting that the maximum temperatures in the Pennsylvanian and Triassic succession were reached during the Triassic, and that the Cenozoic burial (under an extremely low geothermal gradient between 15-20°C/km, Fig. 9B) was not enough to overprint them. An integrated 1D model (Fig. 10, SM 4a and 4b) was carried out in order to estimate the heat flow that accounts from the temperature peaks obtained with this multi-method during the Mesozoic and Cenozoic periods. As previously mentioned, a high heat flow stage is modeled for the Permian-Triassic interval, with maximum values of 90 mW/m^2 coinciding with the rift opening stage (cf. Waples 2001) and a progressive decrease until 70 mW/m^2 at the final stage of post-rift (Fig. 10). These high heat flow values allow us to explain the ZHe ages of Pennsylvanian deposits. Two samples from this interval show a partial reset (S-172, 355-310 Ma) and a complete reset (SVF01, 212 Ma) age compatible with temperatures of 170 °C typical of the lower limit of the ZHePRZ (cf. Reiners et al., 2004, Fig. 5). Individual and multisample modelling show a prolonged stay within the PRZ during the Mesozoic. The 1D Petromod model shows slow cooling during this period that could explain the wide range of AFT ages from the Triassic units.

In order to reach values, close to 100 °C for the Triassic samples close to the top of the section, in this model the Triassic paleotemperature on the surface varies between 70 and 80 °C (Fig. 9A). These values are compatible with the current temperatures measured in the African rift (between 40 and 100 °C, cf. Mwawongo 2010; Dunkley et al. 1993; Wheildon et al., 1994).

The low Miocene geothermal gradient could be explained with heat flow values lower than 30 mW/m^2 (cf. Collo et al., 2017; Wunderlin et al., 2021, Sanchez Nassif et al., 2021). These Miocene heat flow values explain the partial resetting of AHe ages in the strata bounding the Triassic-Cretaceous unconformity (75 °C) and complete resetting of AHe ages in the Triassic basal and Pennsylvannian deposits (> 90 °C).

From the thermal trajectory of 4 horizons obtained in this Petromod model (Top Triassic, Top Ischigualasto, Base Ischichuca, and Top Guandacol), we carry out forward thermal models in the software HeFTy, which allow predicting thermochronological ages using the same parameters of actual samples, namely, Dpar values for AFT data, and eU and grain sizes for (U-Th)/He data. We compare the results of these forward models with AFT and AHe data from sample N148 for the Top Triassic horizon, AFT data of sample SIJ1 and AHe data of sample SVF11 for Top Ischigualasto, AFT data of sample S163

and AHe data of sample S-167 for Top Ischichuca, and AFT and ZHe data of sample S172 and AHe data of sample SVF01 for the Top Guandacol horizon. We ran two models using heat flow values of 22 mW/m^2 and 20 mW/m^2, respectively for the last 10 Myr. (Fig. 11). The predicted ages for both forward models adequately reproduces the observed pattern of reset vs unreset ages for all but sample N148, for which only the hotter model (22 mW/m^2) predict one reset AHe aliquot of 7.1 Ma and 4 older ages for the higher eUand or largest aliquots (Table SM 3). We attribute this pattern to the overprediction of AHe ages for high eU samples that has been identified in the of Flowers et al (2009) radiation damage model (Willet et al, 2017). These results validate the boundary conditions used of the Petromod modeling, as well as reinforce our interpretation of a main thermal peak during the Triassic.

5.5. Local and regional implications of this new thermal history.

Avila et al. (2005; 2006 and references therein) proposed a maximum peak temperature as a result of the synorogenic Miocene overburden of the half-grabens in the nearby Cuyana Basin, and an important change in the late Miocene thermal evolution, associated with the Andean compression that generates a tectonic inversion and uplift of some of the main Triassic depocenters. This maximum temperature peak is even reflected in the maturation of the Triassic organic matter and the generation of hydrocarbons, with the subsequent migration and accumulation in the Cenozoic reservoir rocks in the Cuyana Basin. This was considered as a representative thermal model of the more than ten Triassic backarc depocentres developed during the rifting stage in western Argentina (Avila et al., 2005). However, the model of the thermal evolution of the Ischigualasto-Villa Unión basin presented in this work indicates that the maximum temperatures would have been reached at a stage prior to the deposition of the Cretaceous-Cenozoic sequences, during Triassic rifting. The onset of cooling that our data document at 9-7 Ma is contemporary with the sedimentation of the Mio-pliocene units and suggests that the main overarching mechanism for cooling is the lithospheric refrigeration associated with the Andean flat-slab subduction. The Pampean flat-slab of the Central Andes develops between 27 and 33 °S latitude (Ramos et al., 2002) and spatially overlaps with the northern Triassic depocenter. From geochemistry of volcanic rocks, geophysics and structural studies, in this region the slab arrival is estimated between 10 to 5 Ma (Kay and Mpodozis, 2002; Ramos and Folguera, 2014). This allows us to suggest that this thermal model could be considered for these basins as opposed to the model for the southern Cuyana Basin, which was not affected by the flat subduction

regime during this period (see Fig. 1A and 1B). In addition, stratigraphic and structural cross-cutting relationships based on surface and subsurface data have been used to infer the age of onset of thrusting along the Sierra de Valle Fertil at 6 Ma (Ortiz et al., 2021 and references therein), therefore, as mentioned before, the influence of exhumation on cooling should not be ruled out.

Conclusions

The multi-proxy thermal analysis of the Ischigualasto-Villa Unión Basin carried out in this study allows inferring a complex relation between maximum temperatures and timing in the studied sections. The vitrinite reflectance analysis determines that the maximum temperatures reached by the Triassic and Pennsylvannian levels, with the potential to generate hydrocarbons, are in the oil window (between 0.4 and 1.12% Ro). Likewise, they suggest that the western sections had a similar thermal evolution for coeval horizons along strike, whereas the eastern section indicates substantially lower temperatures for those same sequences. I/S data suggest that the principal heating episode occurred before the Cenozoic sedimentation. In the northern and southern sections, a discontinuity in the illite % in I/S and the ordering types was identified between the Cretaceous-Cenozoic successions and the underlying Triassic units. This interpretation is supported by the thermochronological individual and multisample models, which shows that maximum temperatures would be reached during the Triassic, associated with rifting. Cenozoic re-heating increased the temperatures to values of up to ~110 °C for the base of the section, in Carboniferous rocks. The maximum temperatures recorded at the top of the Triassic sequences suggests that these units would have reached these temperatures even at levels close to the paleosurface with a geothermal gradient close to 40-50 ºC/km. However, within a continental rifting tectonic setting, the high heat flow stage is the most important. High temperatures in the western sector would have rapidly decreased towards the east. The thermal asymmetry of the Triassic rift basin suggests that the main heat source would have been the active fault of the half-graben.

The integrated 1D model allows us to estimate the heat flow for each temporal interval, and to explain the temperature peaks obtained. For the Permian-Triassic interval, a high heat flow stage is modeled (maximum values of 100 mW/m^2) during the rift opening stage and a progressive decrease (80 mW/m^2) at the final stage of post-rift. The Miocene low geothermal gradient could be explained with heat flow values lower than 30 mW/m^2, in accordance with the Andean flat-slab stage widely documented in the region.

This study suggests two different stages of burial and exhumation, highlighting that the maximum temperatures reached by the levels with potential for hydrocarbon generation would have occurred during the Triassic. This contrasts with the previous hypothesis for this depocenter and for neighbouring basins, which share a similar geodynamic history from the Mesozoic to the present, which postulate that the maximum temperatures would have occurred during Cenozoic burial as a result of Andean synorogenic deposition. This new hypothesis leads to rethinking the hydrocarbon exploration strategy, placing greater emphasis on pre-Cenozoic sedimentary targets.

Our study exemplifies that peak heating (Triassic) and the onset of cooling (earliest Late Miocene) cannot be directly associated with peak burial (Cenozoic) and the onset of thrust-induced exhumation (younger than 5 Ma), as it is commonly done in thermochronologic studies in sub-andean basins. Thermal signatures in the Ischigualasto-Villa Unión basin are decoupled from subsidence and exhumation signals, and rather respond to changes in basal heat flow.

References

Aldega, L., & Botti, F., Corrado, S. (2007). Clay mineral assemblages and vitrinite reflectance in the Laga Basin (Central Apennines, Italy): what do they record? *Clays and Clay Minerals, 55 (5)*, 504–518.

Álvarez, O., Nacif, S., Gimenez, M., Folguera, A., & Braitenberg, A. (2014). Goce derived vertical gravity gradient delineates great earthquake rupture zones along the Chilean margin. T*ectonophysics, 622*: 198-215. http://dx.doi.org/10.1016/j.tecto.2014.03.011

ASTM D2797/D2797M-11a (2011). *Standard Practice for Preparing Coal Samples for Microscopical Analysis by Reflected Light.* ASTM International, West Conshohocken, PA. http://www.astm.org/cgi-bin/resolver.cgi?D2797D2797M-11a.

ASTM D7708-14 (2014). *Standard Test Method for Microscopical Determination of the Reflectance of Vitrinite Dispersed in Sedimentary Rocks.* ASTM International, West Conshohocken, PA. www.astm.org/Standards/D7708.htm.

Avila, J.N., Chemise Jr, F., Mallmann, G., Borba, A.W., & Luft, F.F. (2005). Thermal evolution of inverted basins: Constraints from apatite fission track thermochronology in the Cuyo Basin, Argentine Precordillera, *Radiation Measurements* 39, 603-611.

Ávila, J.M., Chemale, F., Mallmann, G., Kawashita, K., & Armstrong, R. (2006). Combined stratigraphic and isotopic studies of Triassic strata, Cuyo Basin, Argentine Precordillera. *Geological Society of America Bulletin 118*: 1088-1098.

Barbarand, J., Carter, A., Wood, I., & Hurford, T. (2003). Compositional and structural control of fission-track annealing in apatite. *Chemical Geology, 198 (1–2)*, 107–137. https://doi.org/10.1016/S0009-2541(02)00424-2

Barker, C. (1996). Thermal modeling of petroleum generation: theory and applications. *Dev. Pet. Sci.* 512.

Bense, F. A., Löbens, S., Dunkl, I., Wemmer, K., & Siegesmund, S. (2013). Is the exhumation of the Sierras Pampeanas only related to Neogene flat-slab subduction? Implications from a multi-thermochronological approach. *Journal of South American Earth Sciences, 48,* 123–144. https://doi.org/10.1016/j.jsames.2013.09.002

Bense, F.A., Wemmer, K., Löbens, S., & Siegesmund, S. (2014). Fault gouge analyses: K-Ar illite dating, clay mineralogy and tectonic significance-a study from the Sierras Pampeanas, Argentina. *Int. J. Earth Sci. 103,* 189–218. https://doi.org/10.1007/s00531-013-0956-7

Bird, K.J.; Burruss, R.C.; & Pawlewicz, M.J. (1999). Thermal maturity. In: *The Oil and gas Resource Potential of the 1002 Area, Arctic National Wildlife Refuge, Alaska.* Pawlewicz M.J., (Ed.). U.S: geological Survey Open File Report 98-34, Washington.

Bossi, G. E. (1977). La Formación Cerro Rajado, provincia de La Rioja. *Acta Geológica Lilloana 14:* 19-40.

Burnham, A.K., & Sweeney, J.J. (1989). A chemical kinetic model of vitrinite reflectance maturation. *Geochimica et Cosmochimica Acta, 53,* 2649-2657.

Burnham, A.K. (2019). Kinetic models of vitrinite, kerogen, and bitumen reflectance. *Organic Geochemistry, 131,* pp. 50-59

Canelo H. N., Sanchez-Nassif, F., Torossian, A. D., Walsh M. B., Cortassa V., Dávila F. M. &, Gimenez M. E. (in press). Structural styles of the Villa Unión-San Isidro basement-involved fold and thrust belt, Northern Ischigualasto-Villa Unión Basin province of La Rioja, Argentina. In: *Andean Structural Styles: A Seismic Atlas*. Zamora Valcarce G, and Mora A (Eds.). Elsevier.

Carlson, W. D., Donelick, R. A., & Ketcham, R. A. (1999). Variability of apatite fission-track anneling kinetics; I, Experimental results. *American Mineralogist, 84 (9),* 1213–1223. https://doi.org/10.2138/am-1999-0901

Carrapa, B., Reyes-Bywater, S., Safipour, R., Sobel, E.R., Schoenbohm, L.M., DeCelles, P. G., Reiners, P.W., & Stockli, D., (2014). The effect of inherited paleotopography on exhumation of the Central Andes of NW Argentina. Geol. Soc. Am. Bull. 126 (1–2), 66–77.

Collo, G., Dávila, F.M., Nóbile, J., Astini, R.A., & Gehrels, G. (2011). Clay mineralogy and thermal history of the Neogene Vinchina Basin, central Andes of Argentina: Analysis of factors controlling the heating conditions. *Tectonics 30,* 1–18. https://doi.org/10.1029/2010TC002841

Collo, G., Dávila, F.M., Teixeira, W., Nóbile, J.C., Sant′ Anna, L.G., & Carter, A. (2015). Isotopic and thermochronologic evidence of extremely cold lithosphere associated with a slab flattening in the Central Andes of Argentina. *Basin Research. 29,* 16–40.

Collo, G., Ezpeleta, M., Dávila, F.M., Giménez, M., Soler, S., Martina, F., Ávila, P., Sánchez, F., Calegari, R., Lovecchio, J., & Schiuma, M. (2018). Basin Thermal Structure in the Chilean-Pampean Flat Subduction Zone. In: *The Evolution of the Chilean-Argentinean Andes.* Folguera, A., Contreras-Reyes, E., Heredia, N., Encinas, A., Iannelli, S.B., Oliveros, V., Dávila, F.M., Collo, G., Giambiagi, L., Maksymowicz, A., Iglesia Llanos, M.P., Turienzo, M., Naipauer, M., Orts, D., Litvak, V.D., Alvarez, O., Arriagada, C. (Eds.), Springer, Cham., United States of America. 537–564. https://doi.org/10.1007/978-3-319-67774-3_21

Dávila, F.M., & Carter, A. (2013). Exhumation history of the andean broken foreland revisited. *Geology 41,* 443–446. https://doi.org/10.1130/G33960.1

Dodson, M. H. (1973). Closure temperature in cooling geochronological and petrological systems. *Contributions to Mineralogy and Petrology, 40(3)*, 259–274. https://doi.org/10.1007/BF00373790

Dumitru, T.A. (1990). Subnormal Cenozoic geothermal gradients in the extinct Sierra Nevada magmatic arc: Consequences of Laramide and Post-Laramide shallow-angle subduction. *Journal of Geophysical. Research. 95*, 4925–4941. https://doi.org/10.1029/JB095iB04p04925.

Dumitru, T.A. (1993). A new computer-automated microscope stage system for fission-track analysis. *Int. J. Radiat. Appl. Instrumentation.* Part 21, 575–580. https://doi.org/10.1016/1359-0189(93)90198-I

Dumitru, T.A., Gans, P.B., Foster, D.A., & Miller, E.L. (1991). Refrigeration of the western Cordilleran lithosphere during Laramide shallow-angle subduction. *Geology 19,* 1145–1148. https://doi.org/10.1130/00917613(1991)019<1145:ROTWCL>2.3.CO;2

Dunkley, P.N.; Smith, M.; Allen, D.J.; & Darling, W.G. (1993) *The geothermal activity and geology of the northern sector of the Kenya Rift Valley*. Nottingham, UK, British Geological Survey, 202pp.

Ehlers, T.A., & Chapman, D.S. (1999). Normal fault thermal regimes: conductive and hydrothermal heat transfer surrounding the Wasatch fault, Utah. Tectonophysics 312 (2), 217–234.

Ehlers, T. A., & Farley, K. A. (2003). Apatite (U-Th)/He thermochronometry: Methods and applications to problems in tectonic and surface processes. *Earth and Planetary Science Letters,* 206(1–2), 1–14. https://doi.org/10.101 6/S0012-821X(02)01069-5

English J.M., Johnston S.T., & Wang, K. (2003). Thermal modelling of the Laramide orogeny: testing the flat-slab subduction hypothesis. *Earth and Planetary Science Letters* 214 (3-4) 619-632

Enkelmann, E., Ridgway, K.D., Carignano, C., & Linnemann, U. (2014). A thermochronometric view into an ancient landscape: Tectonic setting, development, and inversion of the Paleozoic eastern Paganzo basin, Argentina. *Lithosphere; 6 (2)*: 93–107. doi: https://doi.org/10.1130/L309.1

Espitalie, J., Deroo, G, & Marquis, F. (1985). *Rock Eval pyrolysis and its Applications.* Institut Français du Pétrole no. 27299

Farley, K.A. (2002). (U-Th)/He dating: Techniques, calibrations, and applications. Rev. Mineral. Geochemistry 47, 819–844. https://doi.org/10.2138/rmg.2002.47.18

Fitzgerald, P.G. (1994). Thermochronologic constraints on post-Paleozoic tectonic evolution of the central Transantarctic Mountains, Antarctica. Tectonics 13 (4), 818–836.

Fitzgerald, P.G., Fryxell, J.E., & Wernicke, B.P. (1991). Miocene crustal extension and uplift in southeastern Nevada: constraints from fission track analysis. Geology 19 (10), 1013–1016.

Flowers, R.M., Ketcham, R.A., Shuster, D.L., & Farley, K.A. (2009). Apatite (U-Th)/He thermochronometry using a radiation damage accumulation and annealing model. *Geochim. Cosmochim*. Acta 73, 2347–2365. https://doi.org/10.1016/j.gca.2009.01.015

Fosdick, J.C., Carrapa, B., & Ortiz, G. (2015). Faulting and erosion in the Argentine Precordillera during changes in subduction regime: reconciling bedrock cooling and detrital records. *Earth and Planetary Science Letters* 432: 73-83.

Franzese, J.R. & Spalletti, L.A. (2001). Late Triassic-early Jurassic continental extension in southwestern Gondwana: tectonic segmentation and pre-break-up rifting. *Journal of South American Earth Sciences, 14,* 257–270.

Gallagher, K. (2012). Transdimensional inverse thermal history modeling for quantitative thermochronology. *J. Geophys. Res. Solid Earth* 117, 1–16. https://doi.org/10.1029/2011JB008825

Galetto, A.. Georgieva, V., García, V.H., Zattin, M., Sobel, E.R., Glodny, J., Bordese, S., Arzadún, G., Bechis, F., Caselli, A.T., and R. Becchio, R. in press, 2021. Cretaceous and Eocene rapid cooling phases in the Southern Andes (36°-37°S): Insights from low-temperature thermochronology, U-Pb geochronology, and inverse thermal modeling from Domuyo area, Argentina: *Tectonics*

Gans, C. R., Beck, S. L., Zandt, G., Gilbert, H., Alvarado, P., Anderson, M., & Linkimer, L. (2011). Continental and oceanic crustal structure of the Pampean flat slab region, western Argentina, using receiver function analysis: new high-resolution results. *Geophysical Journal International,* 186(1), 45–58. doi:10.1111/j.1365-246x.2011.05023.x

Georgieff, S.M.; Ibañez, L.M.; & Bossi, G.E. (2009). El subsuelo del campo de Talampaya: estratigrafía y evolución tectónica. Cuenca de Ischigualasto- Ischichuca, La Rioja, Argentina. A*cta Geológica Lilloana; 21*, 66 - 76.

Gimenez, M.E., Martinez, M.P., & Introcaso, A. (2000). A Crustal Model based mainly on Gravity data in the Area between the Bermejo Basin and the Sierras de Valle Fkrtil- Argentina. *Journal of South American Earth Sciences, 13,* 275-286

Gleadow, A.J.W., & Duddy, I.R. (1981). A natural long-term track annealing experiment for apatite. *Nuclear Tracks and Radiation Measurements 5,* 169–174. https://doi.org/10.1016/0191-278X(81)90039-1

Green, P. F., Duddy, I. R., Gleadow, A. J. W., Tingate, P. R., & Laslett, G. M. (1985). Fission-track annealing in apatite: Track length measurements and the form of the Arrhenius plot. *Nuclear Tracks and Radiation Measurements (1982), 10 (3),* 323–328.

Guenthner, W. R., Reiners, P. W.,Ketcham, R. A.,Nasdala, L., & Giester, G. (2013). Helium diffusion in natural zircon: Radiation damage, anisotropy, and the interpretation of zircon (U-Th)/He

thermochronology. *American Journal of Science, 313 (3),* 145–198. https://doi.org/10.2475/03.2013.01

Gulbranson, E.L., Ciccioli, P.L., Montañez, I.P., Marenssi, S.A., Limarino, C.O., Schmitz, M.D., & Davydov, V. (2015). Paleoenvironments and age of the Talampaya formation: The Permo-Triassic boundary in northwestern Argentina. *Journal of South American Earth Sciences 63:* 310-322.

Gutscher, M.A., & Peacock,S.M. (2003). Thermal models of flat subduction and the rupture zone of great subduction earthquakes. *Journal of Geophysical Research 108* (B1),2009, 10.1029;

Gutscher, M.A. (2002). Andean subduction styles and their effect on thermal structure and interplate coupling. *Journal of South American Earth Sciences 15:* 3–-10.

Gutscher, M.A., Spakman, W., Bijwaard, H., & Engdahl, E.R. (2000). Geodynamics of flat subduction: Seismicity and tomographic constraints from the Andean margin. *Tectonics 19,* 814–833. https://doi.org/10.1029/1999TC001152

Hackley, P.C., & Lewan, M.D. (2018). Understanding and distinguishing reflectance measurements of solid bitumen and vitrinite using hydrous pyrolysis: implications to petroleum assessment. *American Association of Petroleum Geologists Bulletin 102*, 1119–1140.

Harrison, T. M. (2005). Fundamentals of noble gas thermochronometry. *Reviews in Mineralogy and Geochemistry, 58(1)*, 123–149. https://doi.org/10.2138/rmg.2005.58.5

Hoke, G.D., Giambiagi, L.B., Garzione, C.N., Mahoney, J.B., & Strecker, M.R. (2014). Neogene paleoelevation of intermontane basins in a narrow, compressional mountain range, southern Central Andes of Argentina. *Earth and Planetary Science Letters 406,* 153–164. https://doi.org/10.1016/j.epsl.2014.08.032

Hurford, A. J. (1998). Zeta: The ultimate solution to fission-track analysis calibration or just an interim measure? In: *Advances in Fission-Track Geochronology*, 19–32. Dordrecht: Springer.

International Committee for Coal and Organic Petrology (ICCP) (1998). *The New Vitrinite Classification* (ICCP System, 1994). Fuel 77, 349–358.

International Committee for Coal and Organic Petrology (ICCP) (2001). *The New Inertinite Classification* (ICCP System, 1994). Fuel 80, 459–471.

Jordan, T.E., Allmendinger, R.W., Damanti, J.F., & Drake, R.E. (1993). Chronology of motion in a complete thrust belt: the Precordillera, 30-31°S, Andes Mountains. *The Journal of Geology 101,* 135–156. https://doi.org/10.1086/648213

Jordan, T.E., Schlunegger, F., & Cardozo, N. (2001). Unsteady and spatially variable evolution of the Neogene Andean Bermejo foreland basin, Argentina. *ournal of South American Earth Sciences 14,* 775–798. https://doi.org/10.1016/S0895-9811(01)00072-4

Kay, S.M., & Mpodozis, C. (2002). Magmatism as a probe to the Neogene shallowing of the Nazca plate beneath the modern Chilean flat-slabs. *ournal of South American Earth Sciences 15,* 39–57. https://doi.org/10.1016/S0895-9811(02)00005-6.

Kay, S.M., Mpodozis, C., Ramos, V.A., & Munizaga, F. (1991). Magma source variations for mid-late Tertiary magmatic rocks associated with a shallowing subduction zone and a thickening crust in the central Andes (28 to 33° S). *Special Paper of the Geological Society of America 265*, 113–137.

Ketcham, R. A., Carter, A., Donelick, R. A., Barbarand, J., & Hurford, A. J. (2007). Improved modeling of fission-track annealing in apatite. *American Mineralogist, 92(5–6),* 799–810. https://doi.org/10.2138/am.2007.2281

Ketcham, R. A., Donelick, R. A., & Carlson, W. D. (1999). Variability of apatite fission-track anneling kinetics: III. Extrapolation to geological time scales. *American Mineralogist, 84(9),* 1235–1255. https://doi.org/10.2138/Am.2006.464

Lemos Santos, D., Teixeira, W., Collo, G., & Canelo, H.N. (2018). U–Pb and Sm–Nd constraints on miocene units in the Ischigualasto-Villa Unión foreland basin, Sierras Pampeanas, Argentina: Sedimentary provenance, landscape evolution coupling flat-slab subduction; Pergamon-Elsevier Science Ltd; *Journal of South American Earth Sciences; 90,* 76-93

Lopatin, N.V. (1971). Temperature and geologic time as factors in coalification. Akademiya Nauk SSSR Izvestiya, *Seriya Geologicheskay 3,* 95–106.

López, M.G., Castro De Machuca, B., Flores, D., Malisia, C.I., Fuentes, M.G., & Mulet, V. (2020). Petrografía y geoquímica de la Basanita El Retamo: nueva evidencia del magmatismo triásico en la sierra de Valle Fértil, provincia de San Juan. *Revista de la Asociación Geológica Argentina 77 (2):* 230-243.

Magoon, L.B., & Beaumont, E.A. (1999). Petroleum System. In: *Exploring for oil and gas traps.* American Association of Petroleum Geologists Treatise of Petroleum Geology. Beaumont, E.A., Foster N.H. (Eds). 3.1-3.4.

Makhous, M., & Galushkin, Y.I. (2005). Basin Analysis and Modeling of the Burial, Thermal and Maturation Histories in Sedimentary Basins. Editions Technip, Paris

Malizia, D.C., Reynolds, J.H., & Tabbutt, K.D. (1995). Chronology of Neogene sedimentation, stratigraphy, and tectonism in the Campo de Talampaya region, La Rioja Province, Argentina. *Sedimentary Geology 96,* 231-255

Mancuso, A.C., & Caselli, A T. (2012). Paleolimnology evolution in rift basins: the Ischigualasto–Villa Unión Basin (Central-Western Argentina) during the Triassic. *Sedimentary Geology, 275-276,* 38-54.

Manea, V.C., & Manea, M. (2011). Flat-slab thermal structure and evolution beneath central Mexico. *Pure App Geophys 168,* 1475–-1487.

Marot, M., Monfret, T., Gerbault, M., Nolet, G., Ranalli, G., & Pardo, M. (2014). Flat versus normal subduction zones: a comparison based on 3-D regional traveltime tomography and petrological modelling of

central Chile and western Argentina (29°–35°S), *Geophysical Journal International, 199 (3)* 1633–1654. https://doi.org/10.1093/gji/ggu355

Martina, F., Avila, P., Dávila, F.M., & Parra, M. (2021). Triassic-Jurassic thermal evolution and exhumation of the western Gondwana foreland: Thermochronology and basalt thermobarometry from the Argentine Sierras Pampeanas. *Journal of South American Earth Sciences, 105,* 102956. https://doi.org/10.1016/j.jsames.2020.102956

Melchor, R.N. (2007). Changing lake dynamics and sequence stratigraphy of synrift lacustrine strata in a half-graben: an example from the Triassic Ischigualasto–Villa Unión Basin, Argentina. *Sedimentology, 54:* 1417–1446.

Merriman, R.J., & Frey, M. (1999). Patterns of Very Low- Grade Metamorphism in Metapelitic Rocks. In: *Low Grade Metamorphism.* Frey, M., Robinson, D. (Eds.), Blackwell., Oxford, 61-107

Merriman, R. J., & Peacor, D. R. (1999). Very low grade metapelites: Mineralogy, microfabrics and measuring reaction progress, In: *Low Grade Metamorphism*. Frey M. and Robinson D. (Eds.), Blackwell., Oxford, 10–60.

Meunier, A. (2005). Clays. Springer Berlin. pp: 471.

Milana, J.P. & Alcober, O. (1994). Modelo tectosedimentario de la cuenca triásica de Ischigualasto (San Juan Argentina). *Revista de la Asociación Geológica Argentina 49:* 217-235.

Monetta, A., J. Baraldo, M. Lanzilotta, & Cisneros, H. (1993). Los basaltos del borde oriental de la cuenca de Ischigualasto y su posición estratigráfica. *12° Congreso Geológico Argentino and 2° Congreso de Exploración de Hidrocarburos, 2:* 71-77. Mendoza, Argentina.

Moore, D.M. & Reynolds, R.C. (1997). *X-Ray Diffraction and the Identification and Analysis of Clay Minerals.* 2nd Edn., Oxford University Press, New York, pp: 378.

Mwawongo, G.D. (2010). Geothermal mapping using temperature measurements. *UNU-GTP, GDC and KenGen Congress, Short Course V on Exploration for Geothermal Resources.* Lake Bogoria and Lake Naivasha, Kenya. 13 pp.

Nielsen, S.B., Clausen, O.R., & McGregor, E. (2015). Basin %Ro: A vitrinite reflectance model derived from basin and laboratory data. *Basin Research 29*, 515–536

Ortíz, G., Alvarado, P., Fosdick, J.C., Perucca, L., Saez, M., & Venerdini, A. (2015). Active deformation in the northern Sierra de Valle Fértil, Sierras Pampeanas, Argentina. *Journal South American Earth Sciences 64:* 339-350

Pérez, M.A., Delpiano, V.B., Graneros, D., Breier, K., & Lauría, M. (2011). Cuenca Precordillera: claves exploratorias para el Paleozoico.Áreas Jachal y Niquivil, San Juan, Argentina. In: *Cuencas Argentinas, visión actual. VIII Congreso de Exploración y Desarrollo de Hidrocarburos,* Kozlowsky, E., Legarreta, L., Boll, A., Marshall, P.A. (Eds.), 275-320.

Pickel, W., Kus, J., Flores, D., Kalaizidis, S., Christanis, K., Cardott, B.J., Misz-Kennan, M., Rodrigues, S., Hentschel, A., Hamor-Vido, M., Crosdale, P., & Wagner, N. (2017). Classification of liptinite – ICCP System 1994. *International Journal of Coal Geology 169,* 40–61.

Ramos, V.A. (1970). Estratigrafía y estructura del Terciario en la sierra de los colorados (Provincia de La Rioja), República Argentina. *Revista de la Asociación Geológica Argentina, 25(3),* 359-382.

Ramos, V.A. (1999). Las provincias geológicas del territorio argentino. In: *Geología Argentina*. Caminos, R. (Ed.), Instituto de Geología y Recursos Minerales, Anales 29(3): 41-96

Ramos, V. A., & Folguera, A. (2009). Andean flat-slab subduction through time. *Geological Society of London, Special Publications, 327(1),* 31–54. https://doi.org/10.1144/SP327.3

Ramos, V.A., Cristallini, E.O., & Perez, D. (2002). The Pampean flat-slab of the Central Andes. *Journal of South American Earth Sciences 15:* 59-78.

Reiners, P. W. (2005). Past, present, and future of thermochronology. *Reviews in Mineralogy and Geochemistry, 58(1),* 1–18. https://doi.org/10.2138/rmg.2005.58.1

Reiners, P. W., Spell, T. L., Nicolescu, S. & Zanetti, K. A. (2004). Zircon (U-Th)/He thermochronometry: He diffusion and comparisons with 40Ar/39Ar dating. *Geochimica et Cosmochimica Acta* 68, 1857–1887, https://doi.org/10.1016/j.gca.2003.10.021

Richardson, T., Ridgway, K.D., Gilbert, H., Martino, R., Enkelmann, E., Anderson, M., & Alvarado, P. (2013). Neogene and Quaternary tectonics of the Eastern Sierras Pampeanas, Argentina: Active intraplate deformation inboard of flat-slab subduction. *Tectonics 32,* 780–796. https://doi.org/10.1002/tect.20054

Rossello, E.A., Limarino, C.O., Ortiz, A., & Hernández, N. (2005). Cuencas de los bolsones de San Juan y La Rioja. In: Fronteras Exploratorias de la Argentina. VI Congreso de Exploración y Desarrollo de Hidrocarburos. Chebli, G.A.; Cortiñas, J.S.; Spalletti, L.A.; Legarreta, L; y Vallejo, E.L. (Eds.), 147-174.

Sanchez Nassif, F., Canelo, H., Dávila, F. M., & Ezpeleta, M. (2019). Constraining erosion rates in thrust belts: insights from kinematic modeling of the Argentine Precordillera, Jachal section. *Tectonophysics 758,* 1-11. https://doi.org/10.1016/j.tecto.2019.03.012

Sanchez Nassif, F., Gallagher, K., Ezpeleta, M., Collo, G., Davila, F.M., & Mora, A. (2021). Linking thermochronological data to transient geodynamic regimes; new insights from kinematic modeling and Monte Carlo sampling of thermal boundary conditions. J*ournal of South American Earth Sciences, 105,* 103018, https://doi.org/10.1016/j.jsames.2020.103018.

Schenk, H.J., Horsfield, B., Krooss, B., Schaefer, R.G., & Schwochau, K. (1997). *Kinetics of petroleum formation and cracking, Petroleum and Basin Evolution.* In: Welte, D.H., Horsfield, B., Backer, D.R. (Eds.): Berlin, Springer, p. 233-269.

Schlumberger (2011). User Guide petro Mode 2011.

Sclater, J.G., & Christie, P.A.F. (1980). Continental stretching: An explanation of the Post-Mid-Cretaceous subsidence of the central North Sea Basin. *Journal of Geophysical Research Solid Earth 85,* 3711–3739. https://doi.org/10.1029/jb085ib07p03711

Shuster, D.L., Flowers, R.M., & Farley, K.A. (2006). The influence of natural radiation damage on helium diffusion kinetics in apatite. *Earth and Planetary Science Letters, 249 (3–4),* pp.148-161. https://doi.org/10.1016/j.epsl.2006.07.028.

Siame, L.L., Bellier, O., Sébrier, M., & Araujo, M. (2005). Deformation partitioning in flat subduction setting: the case of the Andean foreland of western Argentina (28°S–33°S), *Tectonics 24,* TC5003, doi:10.1029/2005TC001787

Spalletti, L.A. (2001). *Evolución de las cuencas sedimentarias.* In: Artabe, A.E., Morel, E.M., Zamuner, A.E. (Eds.). El Sistema Triásico en la Argentina. La Plata, Fundación Museo de La Plata "Francisco P. Moreno", 81-101

Środoń, J. (2007). Illitization of smectite and history of sedimentary basins. *Proceedings of the 11th EUROCLAY Conference,* 74-82. Aveiro, Portugal.

Stach, E., Mackowsky, M,, Teichmuller, M., Taylor, G. H., Chandra, D., & Teichmuller, R. (1982). *Textbook of Coal Petrology* (3rd Ed.). Berlin Gebruder Borntraeger

Stevens Goddard, A. L., & Carrapa, B. (2018). Using basin thermal history to evaluate the role of Miocene–Pliocene flat-slab subduction in the southern Central Andes (27° S–30° S). *Basin Research, 30(3),* 564–585. https://doi.org/10.1111/bre.12265

Stockli, D.F. (2005). Application of low-temperature thermochronometry to extensional tectonic settings. Rev. Mineral. Geochem. 58 (1), 411–448.

Stockli, D.F., Farley, K.A., & Dumitru, T.A. (2000). Calibration of the apatite (U-Th)/He thermochronometer on an exhumed fault block, White Mountains, California. Geology 28, 983–986.

Stockli, D.F., Surpless, B.E., Dumitru, T.A., & Farley, K.A. (2002). Thermochronological constraints on the timing and magnitude of Miocene and Pliocene extension in the central Wassuk Range, western Nevada. Tectonics 21 (4).

Sweeney, J. J., & Burnham, A. K. (1990). Evaluation of a simple model of vitrinite reflectance based on chemical kinetics (1). *American Association of Petroleum Geologists Bulletin, 74,* 1559–1570.

Tankard, A.J., Uliana, M.A., Welsink, H.J., Ramos, V.A., Turic, M., França, A.B., Milani, E.J., Brito Neves, B.B.;, Eyles, N., Skarmeta, J., Santa Ana, H., Wiens, F., Cirbián, M., López Paulsen, O., Germs, G.J.B., De Wit, M.J., Machacha, T., & McG. Miller, R. (1995). Structural and tectonic controls of basin evolution in southwestern Gondwana during the Phanerozoic. In: *Petroleum basins of South America*. Tankard, A. J., Suárez Soruco R., Welsink, H. J. (Eds). *American Association of Petroleum Geologists Memoir 62:* 5-52. Tulsa.

Teichmuller, M. (1987). Recent advances in coalification studies and their application to geology. In: *Coal and Coal Bearing Strata: Recent advances.* Scott, A. C. (Ed.) *Geological Society of London, Special Publication, 32,* 127-169.

Tissot, B. P., Pelet, R., & Ungerer, P. (1987). Thermal History of Sedimentary Basins, Maturation Indices, and Kinetics of Oil and Gas Generation, *American Association of Petroleum Geologists Bulletin 71,* 1445-1466.

Tissot, B., & Welte, D. H. (1984). *Petroleum formation and occurrence.* NewYork, Springer-Verlag, 699 p.

Uliana, M.A., Biddle, K.T., & Cerdan, J. (1989). Mesozoic extension and the formation of Argentine sedimentary basins. *American Association of Petroleum Geologists Memoir 46:* 599-614.

Ungerer, P., Burrus, J., Doligez, B., Chenet, P.Y., & Bessis, F. (1990). Basin evaluation by integrated two-dimensional modeling of heat transfer, fluid flow, hydrocarbon generation, and migration. *American Association of Petroleum Geologists Bulletin 74,* 309-335.

Vergés, J., Ramos, V.A., Meigs, A., Cristallini, E., Bettini, B.H. & Cortés, J.M. (2007). Crustal wedging triggering recent deformation in the Andean thrust front between 31º S and 33º S: Sierras Pampeanas-Precordillera interaction. *Journal of Geophysical Research 112,* B03S15, doi:10.1029/2006JB004287

Wangen., M., (1995), The blanketing effect in sedimentary basins*, Basin Research* 7(4):283-298, DOI: 10.1111/j.1365-2117.1995.tb00118.x

Wagner, G. A., Gleadow, A. J. W. W., & Fitzgerald, P. G. (1989). The significance of the partial annealing zone in apatite fission-track analysis: Projected track length measurements and uplift chronology of the transantarctic mountains. *Chemical Geology: Isotope Geoscience Section, 79(4),* 295–305. https://doi.org/10.1016/0168-9622(89)90035-3

Waples, D.W. (2001). A New Model for Heat Flow in Extensional Basins: Radiogenic Heat, Asthenospheric Heat, and the McKenzie Model. *Natural Resources Research, 10,* 227–238. https://doi.org/10.1023/A:1012521309181

Willett., C.D., Fox, M., & Shuster, D.L., (2017), A helium-based model for the effects of radiation damage annealing on helium diffusion kinetics in apatite. *Earth and Planetary Science Letters* 477 (1), 195-204.

Wheildon, J., Morgan, P., Williamson, K.H, Evans, T.R, & Swanber, C.A. (1994). Heat flow in the Kenya rift zone. *Journal of Tectonophysics* 236, 131-149.

Wunderlin, C., Collo, G., Parra, M., Ezpeleta, M., & Toledo, G. (2021). Thermochronological modeling of the Cretaceous-Paleogene sequences in the Cordon de La Flecha Range, La Rioja, Argentina. *Journal of South American Earth Science 105,* 102964. https://doi.org/10.1016/j.jsames.2020.102964

Yáñez, G., Ranero, C., Von Huene, R., & Díaz, J. (2001). Magnetic anomaly interpretation across the southern central Andes (32°-34°S): The role of the Juan Fernandez Ridge in the late Tertiary

evolution of the margin. *Journal of Geophysical Research 106,* (B4): 6325-6345. https://doi.org/10.1029/2000JB900337

Zapata, T.R. & Allmendinger R.W. (1996). Thrust front zone of the Precordillera, Argentina: a thick-skinned triangle zone. *AAPG Bulletin*, 80, 359-381

Zencich, S., Villar, H. J., & Boggetti, D. (2008). Sistema petrolero Cacheuta-Barrancas de la Cuenca Cuyana, provincia de Mendoza, Argentina, In: *Sistemas Petroleros de las Cuencas Andinas, in: Proceedings of the 7th Congreso de Exploración y Desarrollo de Hidrocarburos*. Cruz, C., Rodríguez, J., Hechen, J., and Villar (Eds.), 109–134. Mar del Plata, Argentina.

Zhou, R., Schoenbohm, L. M., Sobel, E. R., Davis, D. W., & Glodny, J. 2017. New constraints on orogenic models of the southern Central Andean Plateau: Cenozoic basin evolution and bedrock exhumation. Geological Society of America Bulletin, v. 129, no. 1/2, p. 152–170; doi: 10.1130/B31384.1

Figure 1. A) Regional topographic map/DEM for location of the study area in relation to the main morphological provinces and the current position of the Pampean flat slab, Argentina. Slab top contours are shown by thin white lines (cf. Gans et al. 2011). B) Distribution and isopach map of Triassic rift basins in central-western Argentina. Note the presence of two preferential alignment of depocenters separated by major thrust. 2A corresponds with the trace of the section shown in Fig. 2A and the rectangle indicates the position of Fig. 2B. Modified after Spalletti (2001).

Figure 2. A) Schematic structural cross section along WSW-ENE line in Fig. 1B. Modified after Ortiz et al (2015) and based on Zapata and Allmendinger (1996) and Canelo et al (in press). B) Geological map of the Ischigualasto-Villa Union Basin The studied stratigraphic sections are shown with black lines (N: Ischichuca-Pagancillo creek; E: Gualo river; S: Ischigualasto National Park).

Figure 3. Stratigraphic columns for the northern, southern and eastern sections (see location in Fig. 2B); %Ro, I/S and thermochronological data from this and previous works are indicated. Sample names in red are from Ortiz et al. (2015) and Fosdick et al. (2015). The green and yellow lines indicate the interpreted location of the upper limit of the partial annealing and retention zones for the AFT and ZHe systems, respectively, based on all paleothermal data available. Red circles indicate changes in the interlayered I/S, from poorly ordered (R0), with illite contents not exceeding 20% to R1 type arrangements, with contents of illite between 65 and 80%.

Figure 4. Thermal models for individual samples. Left panel: Allowed time-temperature paths of the various models (maximum likelihood, maximum posterior, maximum mode and the expected model. Central panel. Observed track lengths (histogram) and their modeled distribution (red curve) with the 95% credible interval (gray lines); for sample S167, in which no track-lengths were measured, it is shown the probability density function of the temperature for the period between 228 and 100Ma, where peak temperatures of ~160°C were attained. Right panel: comparison between the observed and the predicted ages; MTL: Mean track length.

Figure 5. Diagram of stratigraphic thickness vs. thermochronological ages (AFT central ages and single grain Ft-corrected AHe and ZHe ages) used in this study, including published ages from three samples (SFV samples, open symbols) from Ortiz et al (2015) and Fosdick et al. (2015); Tables 3 and 4).

Figure6. Cenozoic peak temperature conditions for individual samples based on inverse thermal modeling. Left panel: Thermal histories for the last 30 Myr. Right panel: Probability density curves for the modeled temperatures in the last 20 Myr, showing most likely maximum temperatures of 70-85 °C and onset of cooling between 15 and 4 Ma.

Figure 7: Multi-sample thermal models without a Triassic - early Jurassic time-temperature constraint for the northern (top) and southern (bottom) sections. Left panel: allowed t-T histories of the expected model. The t-T path of the uppermost sample in each profile is represented by a dark blue line, with the 95% credible interval shown in a light blue envelope; the t-T path of the lowermost sample is shown with a red line and its 95% credible interval with a purple envelope. Intermediate samples are shown in thinner gray lines. The green boxes denote the stratigraphic ages of samples modelled in each section, whereas black boxes are constraints defined based on other geological data, as explained in the text. Central Panel: summary of predictions of the expected model (LL is loglikelihood). Right panel: predicted vs observed ages, showing a good fit for AHe and AFT reset ages and moderate fit for older, partially reset ages.

Figure 8: Multi-sample thermal models similar to those of Figure 7 but adding Triassic-early Jurassic heating for the northern (top) and southern (bottom) sections. Left panel: allowed t-T histories of the expected model. The t-T path of the uppermost top sample in each profile is represented by a dark blue line, with the 95% credible interval shown in a light blue envelope; the t-T path of the lowermost sample is shown with a red line and its 95% credible interval with a purple envelope. The green boxes denote the stratigraphic ages of samples modeled in each section, whereas black boxes are

constraints defined based on other geological data, as explained in the text Intermediate samples are shown in thinner gray lines. Central Panel: summary of predictions of the expected model (LL is loglikelihood). Right panel: predicted vs observed ages, showing a good fit for partially reset ages and moderate fit for older, partially reset ages.

Figure 9. SW-NE schematic sections plotting thermal history of the Ischigualasto – Villa Union Basin. A) Triassic Rift: peak temperatures in the western region (~170°C in the Guandacol Fm), which are close to the main normal fault of the Triassic half-graben, decreased to the east. High geothermal gradient values (40-50°C/km) and paleotemperature on the surface are similar to thermal regimes in current rift basins (cf. Mwawongo 2010; Dunkley et al. 1993; Wheildon et al., 1994). B) Cooling concomitant to sediment accumulation of the Miocene- Pliocene synorogenic strata associated with the variation in the thermal flux in the region during flat subduction regime from approximately 15 Ma. G(P): Guandacol Fm (Pennsylvannian), T-T: Talampaya-Tarjados Fms, I-LR: Ischichuca-Los rastros Fms, I: Ischigualasto Fm, LC: Los Colorados Fm, CR(K): Cerro Rajado Fm (Cretaceous), QM(M): Quebarada del Médano Fm (Miocene), D(M-P): Desencuentro (Miocene-Pliocene).

Figure 10. a) 1D thermal modeling for the Ischigualasto-Villa Union Basin using PetroMod 1D Express software. A heat flow of 90 mW/m2 and a gradual decrease to 70 mW/m2 during the Triassic rift are considered. A heat flow of 70 mW/m2 until 15 Ma and a gradual decrease to 20 mW/m2 from 11 Ma to the present according to the model proposed by Collo et al. (2015) and Wunderlin et al (2021) for the Andean foreland basin. The model shows that maximum temperatures for Pennsylvannian and Permo-Triassic units are reached during the Upper Triassic. Black arrows show sample locations. **b)** Heat flux input conditions, (for more details see table SM 3a and 3b in supplementary material).

Figure 11. Left: thermal trajectory of 4 horizons obtained in our Petromod model. **Right:** forward thermal models in the software HeFTy, which allow predict thermochronological ages and compare the results of these forward models with AFT and AHe data.

Table 1. Vitrinite reflectance values. Individual measurements of %Ro and statics in SM 1c. Rmin% and Rmax %= minimum and maximum value measured in the individual sample, n= number of samples, Sd=standard deviation, Ro%= media value.

	Sample	Depth	Formation	Rmin%	Rmax%	n	Sd	Ro%
Northern Section	N-38	1820	Los Rastros Fm	0.600	0.880	30	0.07	**0.75**
	N-39	1740	Los Rastros Fm	0.500	0.890	29	0.09	**0.75**
	N-40	1610	Los Rastros Fm	0.650	0.940	31	0.08	**0.80**
	N-42	1560	Los Rastros Fm	0.590	0.900	26	0.07	**0.75**
	N-43	1480	Los Rastros Fm	0.660	0.920	23	0.08	**0.81**
	N-44	1410	Ischichuca Fm	0.760	0.930	12	0.05	**0.85**
	N-46	1360	Ischichuca Fm	0.870	1.000	18	0.04	**0.95**
	N-47	1330	Ischichuca Fm	0.710	1.020	21	0.09	**0.89**
	N-48	1300	Ischichuca Fm	0.700	1.040	27	0.09	**0.90**
Eastern Section	E-235 A	395	Los Rastros Fm	0.400	0.570	12	0.05	**0.51**
	E-235 B	390	Los Rastros Fm	0.390	0.570	10	0.05	**0.48**
	E-237	450	Los Rastros Fm	0.320	0.560	11	0.07	**0.43**
	E-258 A	355	Los Rastros Fm	0.610	0.870	23	0.08	**0.76**
	E-258 B	350	Los Rastros Fm	0.690	0.940	24	0.07	**0.81**
Southern Section	S-154	1320	Los Rastros Fm	0.515	0.725	92	0.04	**0.63**
	S-155	1310	Los Rastros Fm	0.464	0.625	98	0.04	**0.53**
	S-156	1300	Los Rastros Fm	0.432	0.747	65	0.08	**0.55**
	S-157	1290	Los Rastros Fm	0.432	0.722	110	0.06	**0.53**
	S-158	1270	Los Rastros Fm	0.429	0.707	112	0.06	**0.56**
	S-159	1230	Los Rastros Fm	0.426	0.777	70	0.07	**0.55**
	S-161	1110	Los Rastros Fm	0.463	0.759	78	0.07	**0.59**
	S-162	1090	Ischichuca Fm	0.559	0.804	105	0.05	**0.67**
	S-164	1035	Ischichuca Fm	0.603	0.876	103	0.05	**0.69**
	S-165	975	Ischichuca Fm	0.648	0.962	102	0.07	**0.83**
	S-166	960	Ischichuca Fm	0.681	0.936	71	0.07	**0.81**
	S-167	940	Ischichuca Fm	0.570	0.831	33	0.08	**0.72**
	S-172	480	Guandacol Fm	0.672	0.971	10	0.08	**0.82**
	S-174	80	Guandacol Fm	0.921	1.296	69	0.09	**1.12**
	S-175	50	Guandacol Fm	0.980	1.297	69	0.80	**1.14**

Table 2. Mineralogical identification of the clay mineral fraction. For the I/S characterization the illite proportions in the I/S were established for all samples in each of the sections cf. Moore and Reynolds (1997). Corr: corrensite, Ilt/M: illite/mica, Chl: chlorite, Kaol: kaolinite, Tr: traces?: doubtful presence.

Unit	Sample	Location		Depth	Illite-Smectite Interstratifieds			Corrensite	Illite/Mica	Chlorite	Kaolinite
		Lat	Long		Smectite	I/S	Ord.	% Illin I/S				
Northern Section											
Qda Medano Fm	**N018A**	S 29° 38.064	W 68° 13.016	4050		•	R0	15		•		
Cerro Rajado Fm.	**N017A**	S 29° 39.559	W 68° 15.836	3980		•	R0	5	Tr	•	Tr	
	N016A	S 29° 41.027	W 68° 16.997	3930		•	R0	30		•	Tr	
	N014A	S 29° 41.583	W 68° 16.827	3880		•	R0	20		•	•	
	N015A	S 29° 41.895	W 68° 16.975	3850		•	R0	5		•	Tr	
Los Colorados Fm.	**N004A**	S 29° 41.554	W 68° 17.585	3550		•	R1	65		•		
	N002B	S 29° 41.742	W 68° 17.699	3500		•	R0	5		•		
	N013A	S 29° 42.007	W 68° 17.563	3460		•	R1	65		•		
	N012A	S 29° 42.258	W 68° 17.811	3120		•	R1	65		•		
Ischigualasto Fm.	**N010A**	S 29° 42.459	W 68° 17.820	2890		•	R1	65		•		
	N007B	S 29° 42.693	W 68° 17.756	2680		Tr				•		
	N006A	S 29° 42.739	W 68° 18.345	2600		•	R1	65		•		•
	N005C	S 29° 42.780	W 68° 18.606	2250		•	R1	65		•		Tr
Ischichusca Fm.	**N38**	S29° 38.458	W68° 23.623	1900		Tr				•	•	•

	N39	S29° 38.356	W68° 23.644	1860	Tr				•	•	•	
	N40	S29° 38.211	W68° 23.680	1820	•	R3	85		•	•	•	
	N42	S29° 38.381	W68° 24.067	1700	•	R1	75		•	•	•	
	N43	S29° 38.256	W68° 24.355	1550	•	R3	85		•	•	•	
	N44	S29° 38.070	W68° 24.303	1460	•	R1	75		•	•		
	N48	S29° 37.995	W68° 24.387	1420	•	R3	85		•	•		
	N47	S29° 37.887	W68° 24.301	1380	•	R3	85		•			
	N46	S 29° 37.768	W68° 24.319	1330	Tr				•	?		
Southern section												
Desencuentro Fm.	**S296**	S 29° 57.699	W 67° 52.418	4100	•	R0	20		•	•		
Río Mañero Fm.	**S295**	S 29° 57.880	W 67° 52.485	3450	•	R0	5		•			
	S294	S 29° 58.289	W 67° 52.569	3420	•	R0	25		•			
	S293	S29° 58.565	W 67° 52.435	3320	•	R0	10		•			
	S292	S29° 58.895	W 67° 52.449	3260	•	R0	20		•			
	S291	S 29° 59.067	W 67° 52.604	3200	•	R0	5		•			
Los Colorados Fm.	**S290**	S 29° 59.126	W 67° 52.645	3150	•	R0	20		•	•		
	S289	S 29° 59.310	W 67° 52.813	2720					•	•		
	S288	S 29° 59.447	W 67° 53.209	2610	•	R0			•			Tr
	S287	S 29° 59.676	W 67° 53.650	2500	•	R0	5	Tr	•	Tr		
	S284	S 30° 0.236	W67° 54.198	2360	Tr				•			

	S279	S 30° 0.326	W 67° 54.513	2220		•	R1	65		•		•
	S280	S30° 0.352	W 67° 54.447	1910		•	R1	55		•		•
	S283	S30° 0.316	W 67° 54.621	1850		•	R1	65		•		•
	S151	S30° 4.585	W67° 53.981	1750		•	R0	5				
Ischigualasto Fm.	**Sij6**	S 30° 4.426	W 67° 54.288	1720	•					•		
	Sij5	30° 4.485	W 67° 54.763	1650	•					•		•
	Sij4	S30° 4.694'	W 67° 54.898	1580	•					•		Tr
	Sij3	S 30° 5.371	W 67° 55.145	1520	•					•		Tr
	Sij2	S 30° 5.318	W 67° 55.601	1440	•				Tr	•	Tr	•
	Sij1	S 30° 5.279	W 67° 55.854	1400	•					•	Tr	•
Ischichuca Fm./Los Rastros Fm.	**S153**	S 30° 5.557	W 67° 56.061	1355		•	R1	65		•		•
	S154	S 30° 5.780	W 67° 56.050	1320						•		•
	S155	S 30° 5.807	W 67° 56.465	1310		•	R1	75		•		•
	S156	S 30° 5.851	W 67° 56.899	1300		•	R1	75		•	Tr	•
	S157	S 30° 6.137	W 67° 57.206	1290		•	R3 ?			•	Tr	•
	S158	S 30° 6.149	W 67° 57.535	1270		•	R3 ?			?		•
	S159	S 30° 6.404	W 67° 57.739	1230		•	R1	75		•		Tr
	S160	S 30° 6.304	W 67° 57.826	1160		•	R1	75		•		Tr
	S161	S 30° 6.197	W 67° 57.940	1110		•	R1-R3 ?			•	Tr	Tr
	S162	S 30° 6.650	W 67° 57.935	1090		•	R1-R3 ?			•		•

	S163	S 30° 6.754	W 67° 58.288	1060							
	S164	S 30° 7.180	W 67° 58.257	1035	•	R1-R3 ?		•		•	
	S165	S30° 7.378	W 67° 58.808	975	•	R1	75	•		•	
	S166	S 30° 7.734	W 67° 59.391	960	•	R1	75	•	Tr	•	
	S167	S 30° 7.683	W 67° 59.578	940	•	R3	85	•	Tr	•	
	S168	S 30° 7.836	W 67° 59.820	860	•	R1	70	•		Tr	
	S170	S 30° 7.877	W 67° 59.891	810	•	R1	75	•		Tr	
Tarjados Fm.	**S171**	S 30° 7.820	W 68° 0.044	750	•	R1	75	•		Tr	
	S172	S 30° 8.429	W 68° 1.691	480	•	R1	75	•		Tr	
Guandacol Fm.	**S174**	S 30° 9.253	W 68° 2.527	80				?	•		
	S175-30	S30° 9.264'	W 68° 2.599	50				•	•	Tr	
	S175	S30° 9.355	W 68° 2.731	50				•	•	Tr	
				Eastern section							
Ischichuca Fm. / Rio Gualo Fm.	**E237**	S29.87018	W67.71114	480	•	R0	30	•		•	
	E235B	S29.82251	W67.81107	440	•	R0	25	•		•	
	E235A	S29.82251	W67.81107	420	•	R0	20	•		•	
	E258B	S29.83276	W67.80913	360	•	R0	45	•		•	
	E258A	S29.83276	W67.80913	330	•	R0	50	•		•	
	E266	S29 50.094	W67 47.661	300	•	R0	45	•		•	

Table 3: Apatite fission-track data

Sample	Lat (°)	Long(°)	Elev (m)	Strat. Unit	Strat. Age (Ma)	Strat. Depth (m)	N° of grains	Rho-S (NS)[a]	Rho-I (NI)[a]	Rho-D (ND)[b]	Dpar (μm)	SD (μm)	Age (Ma)	±1σ Error	U (ppm)	P(χ^2)[c]	Length (μm)	Error (μm)	SD (μm)	N° of lengths
North																				
N-150	29.6786	68.28150	980	Cerro Rajado	85 ± 15	3750	25	21.454 (1958)	22.627 (2065)	17.520 (8332)	1.71	0.36	67.4	9.1	47	0.0	10.70	0.28	2.16	61
N-148	29.6894	68.2911	977	Los Colorados	212 ± 5	3500	24	35.428 (2321)	28.758 (1884)	16.779 (8332)	1.84	0.33	78.1	4.5	65	0.0	11.18	0.27	2.71	102
N-145	29.7029	68.2963	966	Los Colorados	215 ± 4	3380	23	10.655 (1187)	5.247 (584)	16.423 (8332)	1.69	0.31	137.1	18.9	12	0.0	12.14	0.32	1.77	31
N-005B	29.71550	68.2983	958	Ischigualasto	225 ± 2	2000	3	33.661 (359)	28.035 (299)	16.423 (8332)	1.84	0.81	56.3	15.8	62	0.4	ND	ND	ND	ND
N-051[e]	29.5349	68.40440	1275	Guandacol	310 ± 4	300	21	2.146 (281)	27.292 (3574)	25.219 (16308)	1.76	0.35	9.3	1.5	41	0.0	ND	ND	ND	ND
South																				
S-IJ1	30.0872	67.9322	1244	Ischigualasto	228 ± 4	1450	4	4.988 (76)	5.120 (78)	18.903 (8332)	1.66	0.29	68.3	11.6	10	57.2	ND	ND	ND	ND
S-163	30.1045	67.9603	1200	Los Rastros	230 ± 2	1050	19	9.260 (273)	9.080 (285)	18.228 (8332)	1.99	0.44	79.4	19.1	19	0.0	12.52	0.53	1.40	7
S-167[e]	30.1476	67.9744	1384	Ischichusca	232 ± 3	950	10	8.708 (335)	17.650 (679)	25.357 (16308)	1.8	0.28	63.1	18.1	26	0.0	ND	ND	ND	ND
S-172	30.1359	68.0268	944	Guandacol	305 ± 4	450	17	2.999 (159)	27.574 (1462)	18.530 (8332)	1.61	0.16	8.6	1.6	56	0.0	12.24	0.08	0.11	2

a RhoS and Rho I are the spontaneous and induced tracks density measured, respectively (x 10^5 tracks/cm^2). NS and NI are the number of spontaneous and induced tracks counted for estimating RhoS and RhoI, respectively

b RhoD is the induced track density measured in the external mica detector attached to CN1 dosimetry glass (x 10^5 tracks/cm^2). ND is the number of induced tracks counted in the mica for estimating RhoD.

c ($\chi 2$) (%) is the chi-square probability (Galbraith, 1981; Green, 1981). Values greater than 5% are considered to pass this test and represent a single population of ages

d Pooled (central) age reported for ages that pass (fail) the c2 test

e Age calculations used a Zeta factor of 80.2 ± 2.1. A value of 74.5 ± 4.0 was use for the remaining analyses

Table 4: (U-Th-Sm)/He data

Sample / Aliquot	Lat	Long	Elev (m)	Unit	Age (Ma)	Strat. Depth (m)	mineral	Ft-corrected age (Ma)	2s (Ma)	U (ppm)	Th (ppm)	147Sm (ppm)	[U]e (ppm)	Th/U	He (nmol/g)	Mass (µg)	Ft	ESR (µm)	Grain dimensions (µm)		
																			L	W	W2
Northern Section																					
N-150	29.67856	68.28150	980	Cerro Rajado	85 ± 15	3750															
N-150-1							Apatite	3.1	0.3	12.2	38.0	20.6	21.1	3.2	0.24	2.1	0.66	44.8	157.0	75.8	71.6
N-150-2							Apatite	2.8	0.7	5.9	31.5	16.6	13.3	5.5	0.12	1.4	0.61	38.5	139.6	67.5	58.2
N-150-3							Apatite	10.0	1.9	4.7	20.3	33.8	9.5	4.4	0.30	1.0	0.56	34.5	120.2	58.2	55.4
N-150-4							Apatite	1.9	0.3	6.0	25.3	20.6	12.0	4.3	0.09	3.1	0.72	52.4	146.4	97.6	86.0
N-148	29.68939	68.29106	977	Los Colorados	212 ± 5	3500															
N-148-1							Apatite	6.7	1.9	4.6	30.1	8.1	11.7	6.8	0.21	0.6	0.50	28.6	124.2	46.3	43.9
N-148-2							Apatite	43.6	0.8	15.2	61.5	49.0	29.6	4.2	5.37	5.7	0.76	63.0	210.3	105.1	105.0
N-148-3							Apatite	35.1	1.1	8.5	12.0	2.0	11.3	1.5	1.53	2.8	0.71	51.1	136.2	97.4	84.3
N-148-4							Apatite	10.2	0.9	9.5	17.5	20.7	13.6	1.9	0.51	1.4	0.67	40.0	120.9	81.6	55.3

N-148-5							Apatite	13.6	0.5	20.6	71.4	39.0	37.3	3.6	1.72	1.3	0.62	38.3	135.6	65.2	60.5
N-145	29.70286	68.29628	966	Los Colorados	215 ± 4	3380															
N-145-1							Apatite	4.1	0.6	2.7	10.2	14.1	5.1	3.9	0.08	2.4	0.69	47.7	152.6	89.0	71.8
N-145-2							Apatite	9.2	0.3	1.8	13.8	15.7	5.0	8.1	0.23	25.1	0.89	107.5	257.2	211.0	186.2
N-145-3							Apatite	19.9	0.9	3.2	14.1	27.6	6.5	4.6	0.54	4.2	0.74	57.8	169.4	102.2	97.4
N-145-4							Apatite	6.6	0.5	1.4	14.5	20.1	4.8	10.7	0.14	6.5	0.76	63.0	261.4	102.8	97.4
N-145-5							Apatite	19.5	0.3	6.5	20.9	29.6	11.4	3.3	0.95	6.7	0.78	68.1	187.6	129.8	109.8
N-051	29.53488	69.4044	1275	Guandacol	310 ± 4	300															
N-051-1							Apatite	4.0	0.1	54.6	134.0	30.2	86.0	2.5	1.54	12.0	0.82	83.7	206.6	151.5	154.4
N-051-2							Apatite	2.6	0.1	15.8	143.1	19.8	49.4	9.4	0.51	3.8	0.74	56.6	151.3	115.2	85.9
N-051-3							Apatite	2.4	0.1	1.2	86.2	11.5	21.4	76.4	0.24	15.3	0.83	90.4	238.0	159.4	163.3
N-051-4							Apatite	2.5	0.1	10.8	116.4	10.8	38.1	11.2	0.38	4.3	0.75	59.1	154.6	104.2	107.3
Southern Section																					
S-167	30.14756	67.97442	1384	Ischichusca	232 ± 3	950															

S-167-1							Apatite	3.3	0.3	8.3	36.6	18.2	16.9	4.6	0.21	2.2	0.68	47.3	123.6	91.1	78.2
S-167-2							Apatite	3.9	0.5	0.7	24.9	9.4	6.5	37.5	0.10	3.8	0.72	53.6	202.2	97.8	75.8
S-167-3							Apatite	8.1	0.3	17.4	71.8	27.4	34.3	4.3	1.12	4.0	0.74	58.2	142.0	106.5	106.8
S-167-4							Apatite	3.6	0.2	6.2	94.3	15.3	28.4	15.6	0.42	4.5	0.75	60.9	141.8	123.9	103.8
S-172	30.13589	68.02681	944	Guandacol	305 ± 4	450															
S-172-1							Zircon	314.0	4.1	122.0	39.1	0.2	131.2	0.3	161.98	3.6	0.71	41.5	178.9	62.6	68.7
S-172-2							Zircon	281.5	4.6	90.9	71.6	0.4	107.7	0.8	114.07	2.6	0.68	37.9	146.0	71.3	54.0

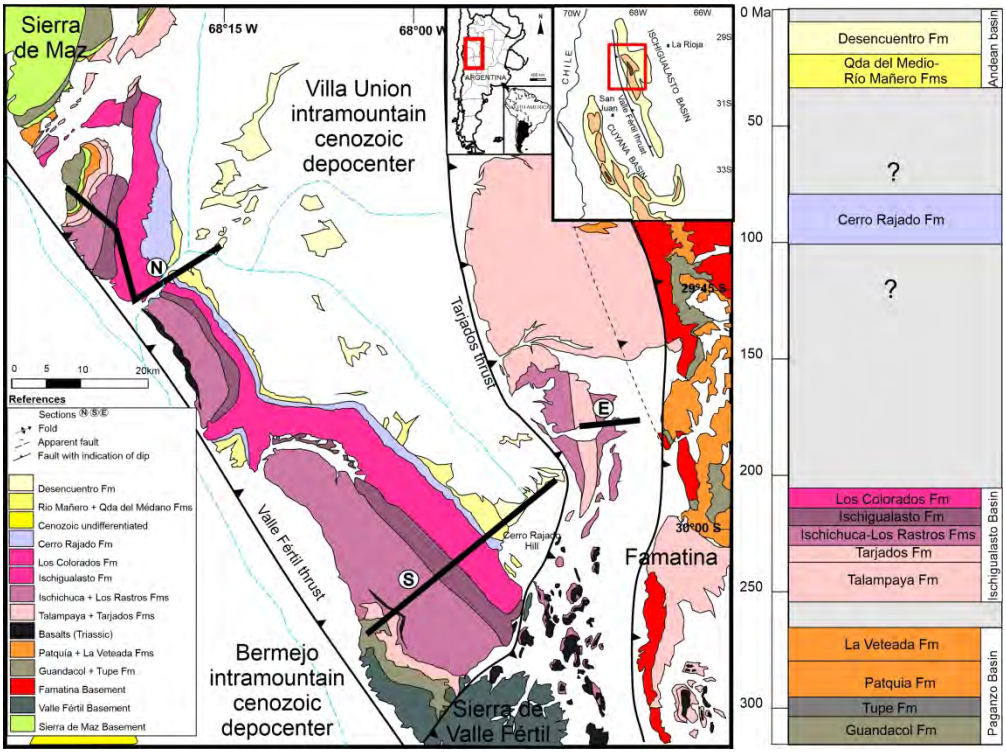

248x185mm (300 x 300 DPI)

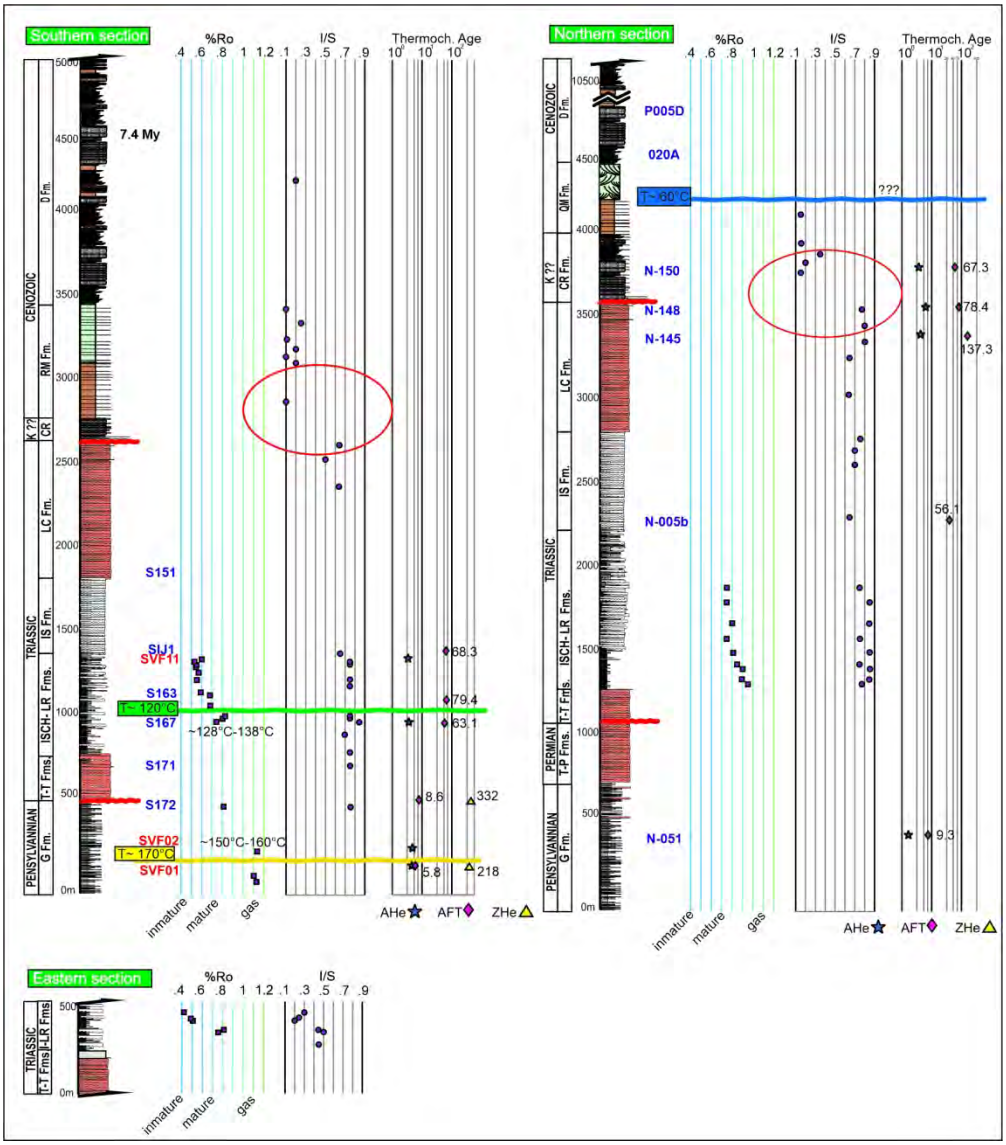

160x182mm (300 x 300 DPI)

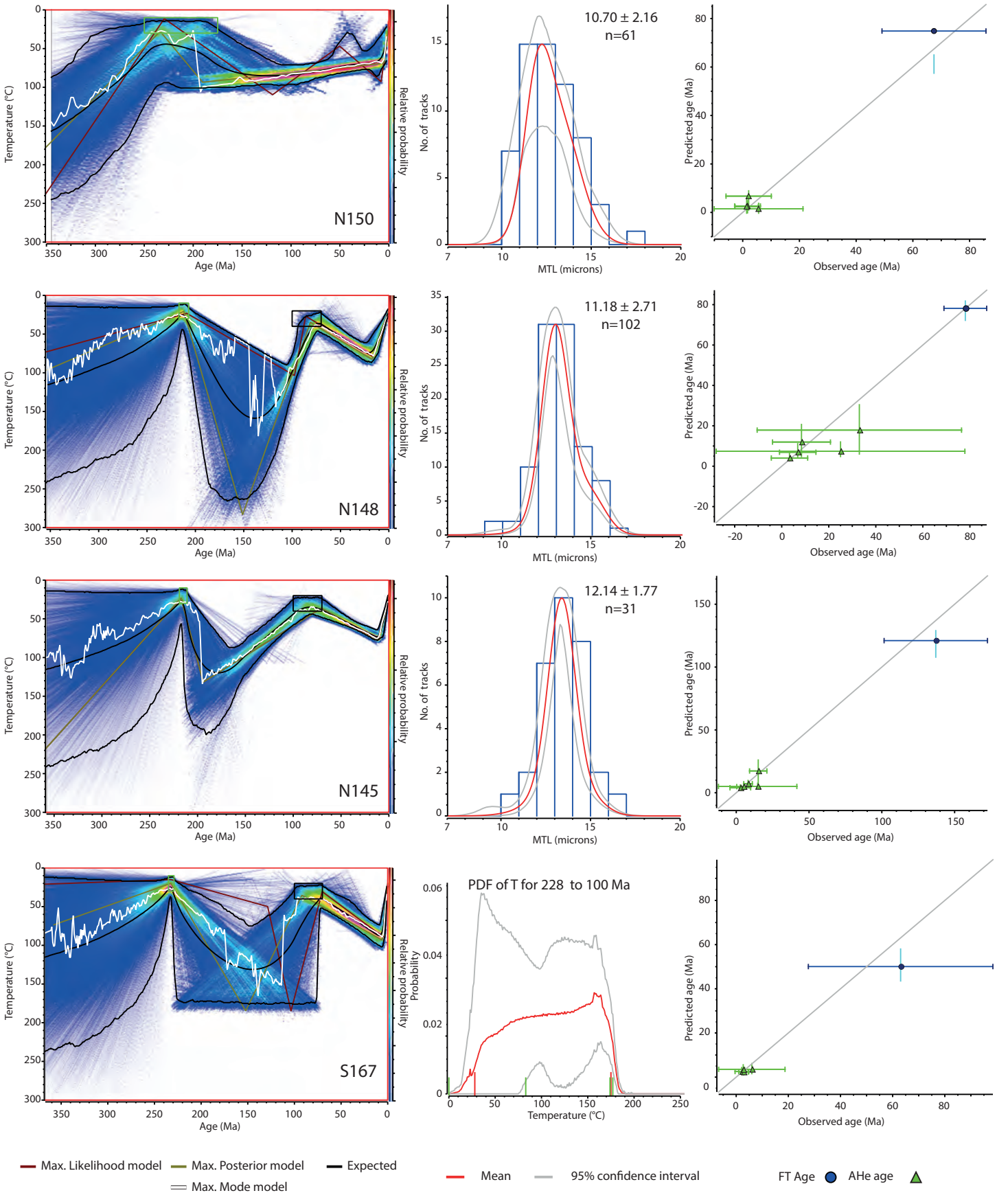

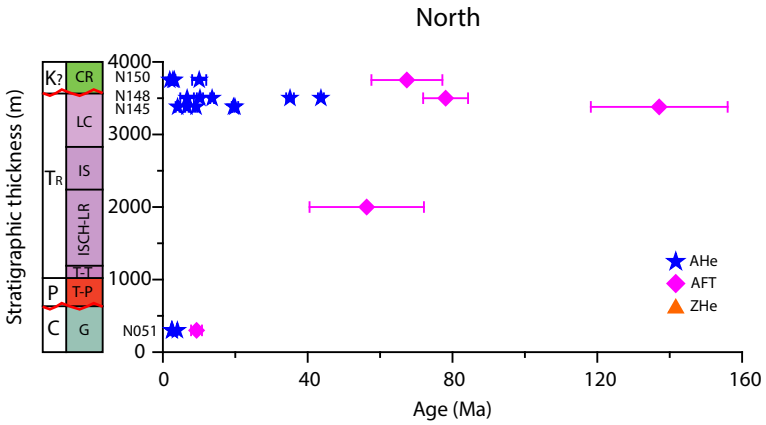
North
Stratigraphic thickness (m)
K?
CR
LC
TR
IS
ISCH-LR
T-T
P
T-P
C
G
4000
3000
2000
1000
0
N150
N148
N145
N051
AHe
AFT
ZHe
0
40
80
120
160
Age (Ma)

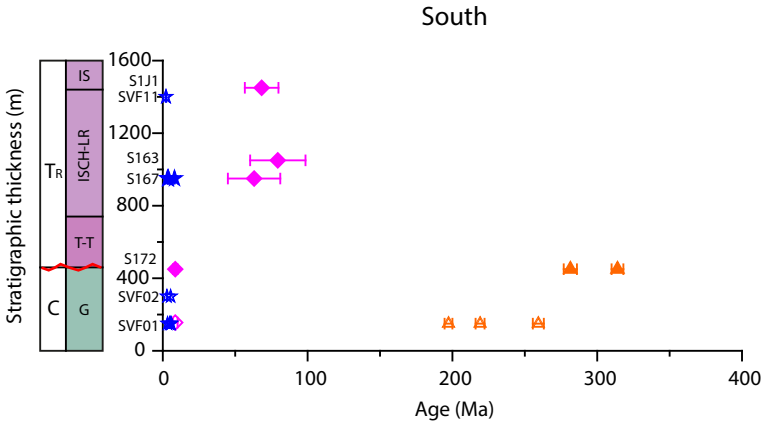
South
Stratigraphic thickness (m)
IS
TR
ISCH-LR
T-T
C
G
1600
1200
800
400
0
S1J1
SVF11
S163
S167
S172
SVF02
SVF01
0
100
200
300
400
Age (Ma)

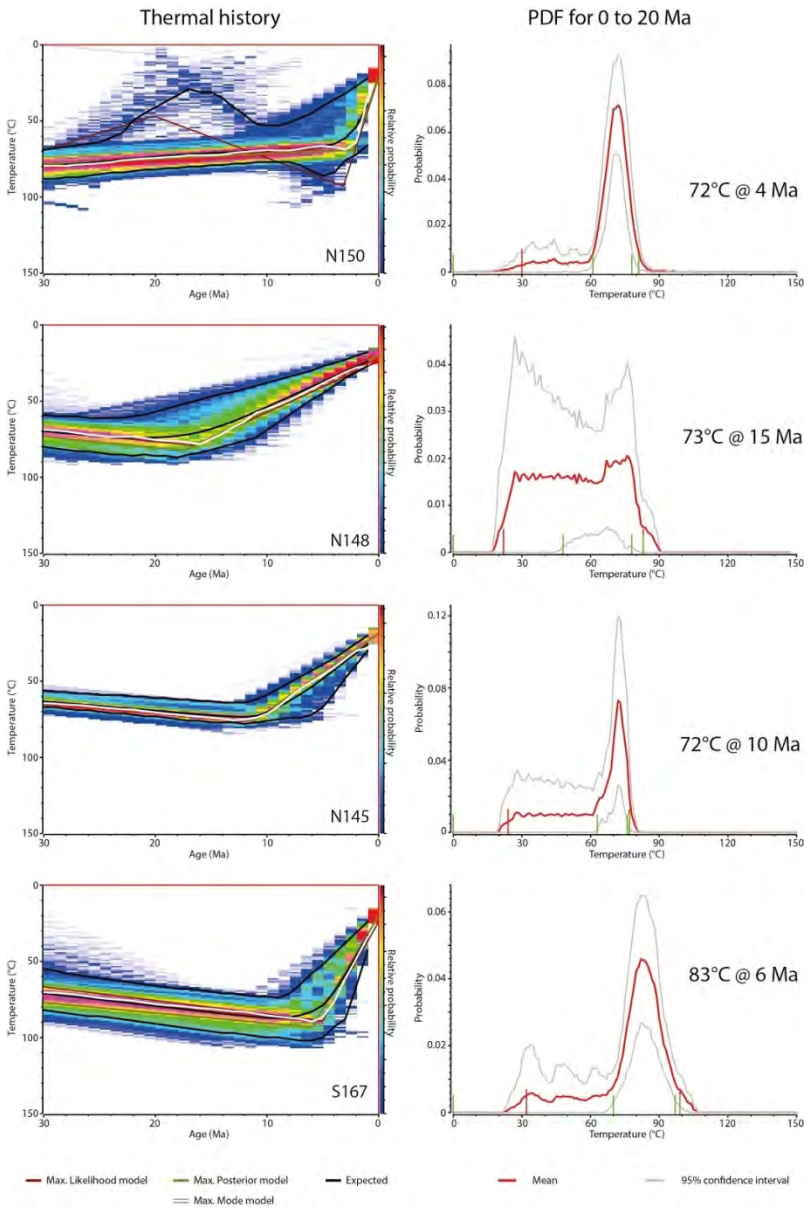

376x564mm (72 x 72 DPI)

Thermal History

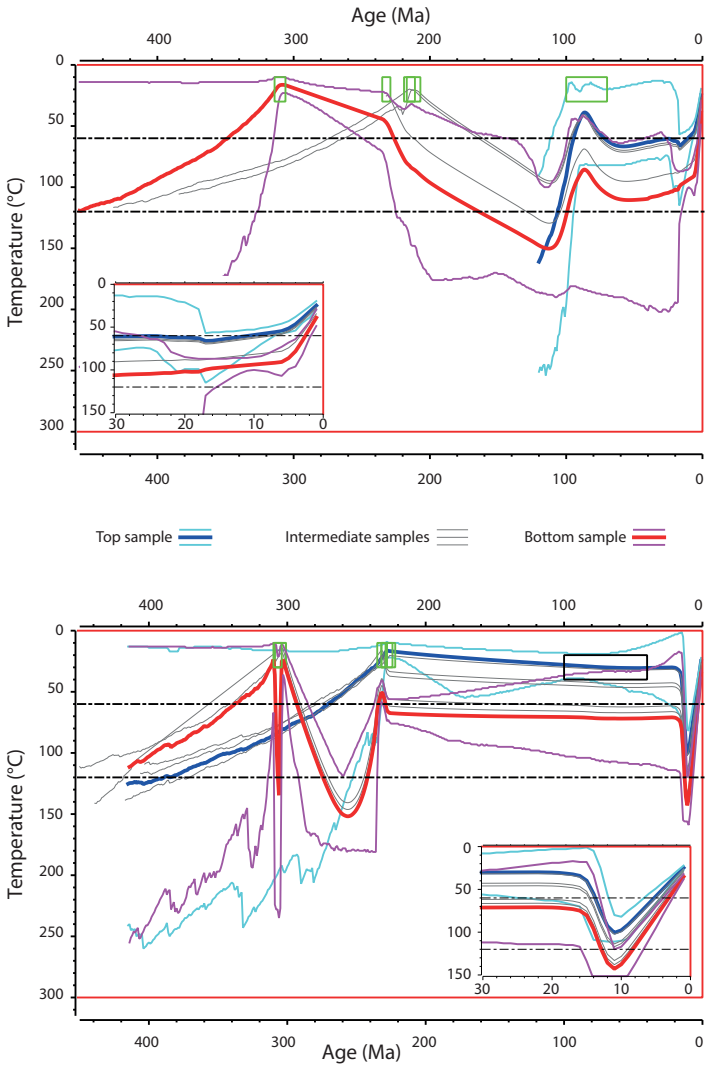

Model predictions vs observations

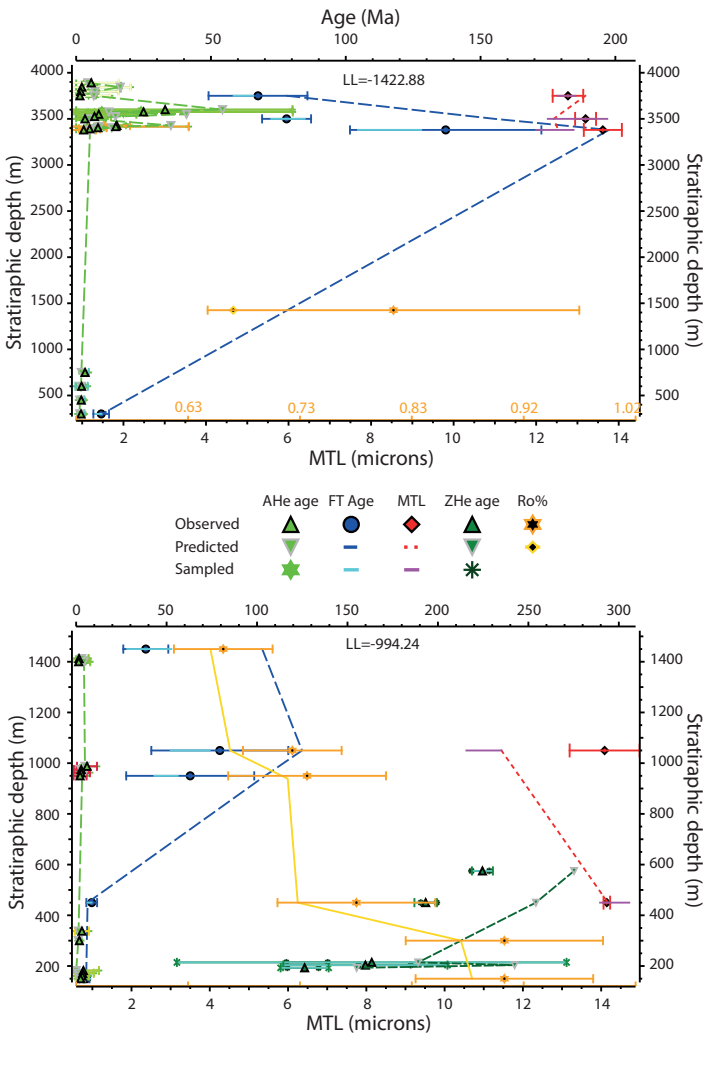

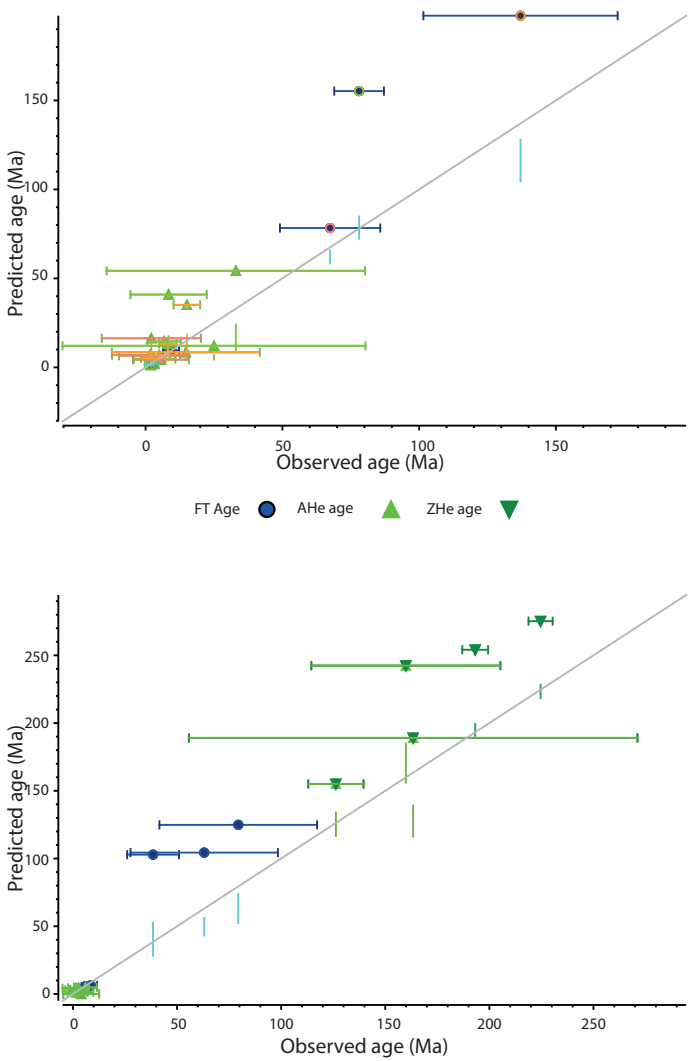

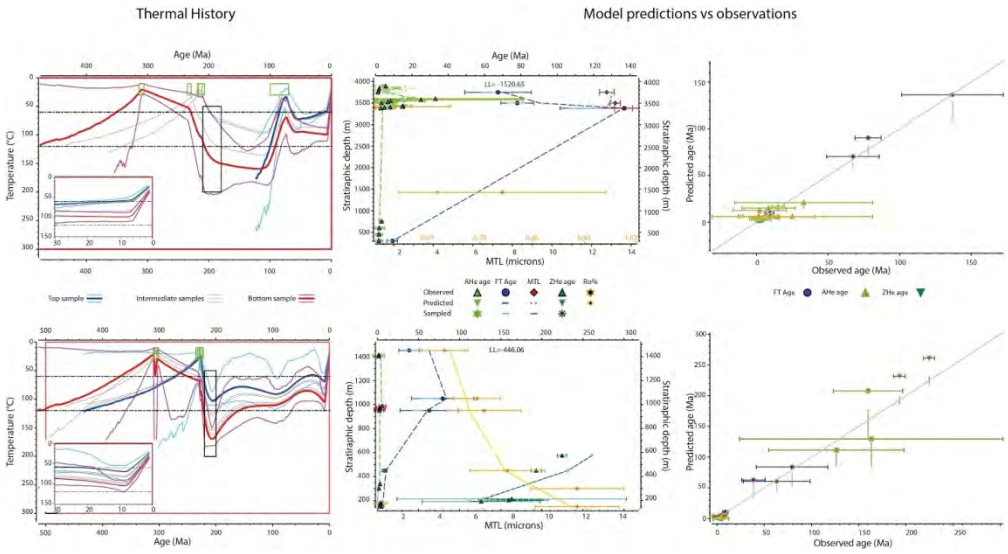

564x306mm (72 x 72 DPI)

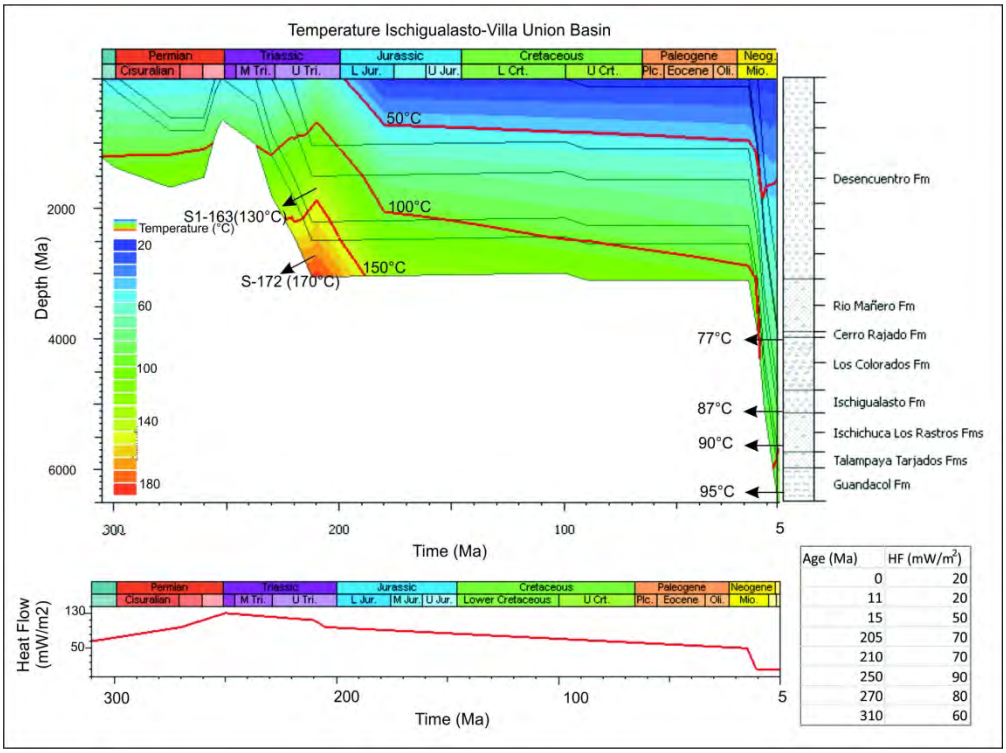

171x127mm (300 x 300 DPI)

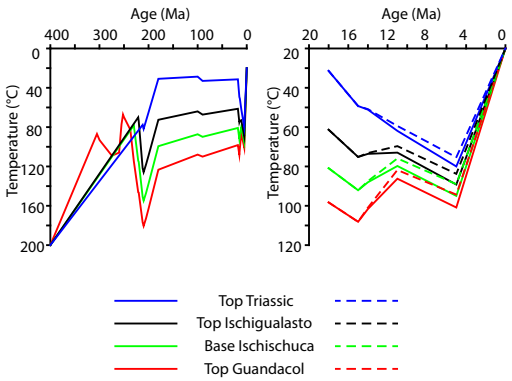
Age (Ma)
400 300 200 100 0
Age (Ma)
20 16 12 8 4 0
Temperature (°C)
0 40 80 120 160 200
Temperature (°C)
20 40 60 80 100 120
Top Triassic
Top Ischigualasto
Base Ischischuca
Top Guandacol

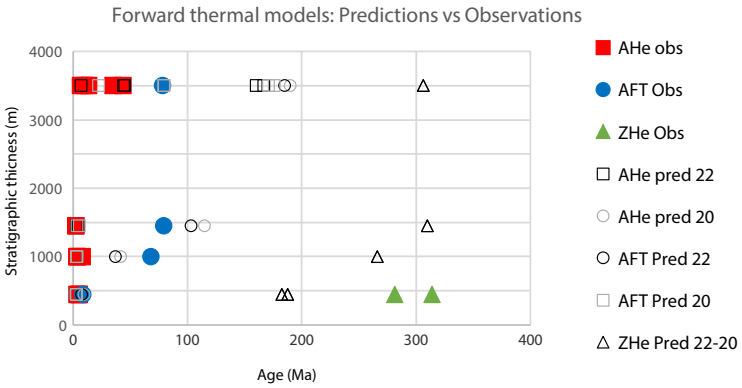
Forward thermal models: Predictions vs Observations
Stratigraphic thicness (m)
4000
3000
2000
1000
0
0 100 200 300 400
Age (Ma)
AHe obs
AFT Obs
ZHe Obs
AHe pred 22
AHe pred 20
AFT Pred 22
AFT Pred 20
ZHe Pred 22-20